Stefan Lengauer, BSc

SLR Validation for Kinematic Orbit Determination

Master's Thesis
to achieve the university degree of
Diplom-Ingenieur
Master's degree programme: Space Sciences and Earth from Space

submitted to

Graz University of Technology

Supervisor
Univ.-Prof. Dr.-Ing. Torsten Mayer-Gürr

Institute of Geodesy

AFFIDAVIT

I declare that I have authored this thesis independently, that I have not used other than the declared sources/resources, and that I have explicitly indicated all material which has been quoted either literally or by content from the sources used. The text document uploaded to TUGRAZonline is identical to the present master's thesis.

Date Signature

Kurzfassung

Satellite Laser Ranging ist eine geodätische Methode aus dem Bereich der Satellitengeodäsie, die für die Distanzmessung die Zweiwegelaufzeit eines Laserpulses verwendet. Die Distanz erhält man durch Halbierung der Flugzeit und Multiplizierung mit der Lichtgeschwindigkeit. Um eine Messung zu erreichen, die die reale Distanz möglichst genau annähert, müssen zusätzliche Korrekturterme berücksichtigt werden, welche die Lichtbrechung in der Atmosphäre, konstante Offsets in den Satelliten- und Bodensystemen, Stationsbewegungen aufgrund von Gezeitenkräften und relativistische Effekte berücksichtigen. Durch präzise Modellierung all dieser Faktoren sind gegenwärtig Messgenauigkeiten von wenigen Zentimetern möglich.

Im Zuge dieser Arbeit wurde Mehrzweckgeodäsiesoftware (GROOPS) des Institute of Geodesy (IfG) der Technischen Universität Graz um ein Modul erweitert dass es erlaubt SLR Messungen, die im Consolidated Ranging Data Dateiformat vorliegen, einzulesen und aus diesen Distanzmessungen und zugehörige Epochen zu extrahieren. Die bereits genannten Korrekturterme wurden durch diverse Modelle abgeschätzt. Zusätzlich is es mit der Software möglich Dateien mit Orbitlösungen zu laden, um zusammen mit der exakten Stationsposition auf der Erdoberfläche, eine vorhergesagte Distanz zu errechnen. Für die Validierung wird der Unterschied von der beobachteten Distanz zu der vorhergesagtenbetrachtet.

Ausgiebige Tests wurden mit den kinematischen Orbits der GRACE und Swarm Satelliten durchgeführt welche von Herrn Dr. Zehentner im Zuge seiner Dissertation berechnet wurden. Zusätzlich wurden Ergenbisse mit den Ergebnissen der TU Delft und dem Astronomical Institute der Universität Bern verglichen.

Abstract

Satellite Laser Ranging is a geodetic technique from the field of satellite geodesy, which uses the two way travel time of a laser pulse as a means of range determination. The distance can be obtained by dividing the time of flight and multiplying it with the speed of light. To obtain a distance measurement, which is close to the actual distance several correction terms accounting for the refraction in the atmosphere, constant offsets on the satellite and on the ground station, displacement of the station due to tidal forces and relativistic effects have to be estimated. With all corrections applied accuracies in the range of few centimeters are currently possible with observations of geodetic satellites.

Within the scope of this thesis, the in-house multi-purpose geodetic software (GROOPS) of the Institute of Geodesy (IfG) at Graz Technical University was extended by a module capable of reading SLR observations given in the Consolidated Ranging Data file format and extract the range measurement with its observation epoch. Models have been implemented to estimate the mentioned error terms in order to get a range measurement as accurate as possible. Additionally, the software is able to read orbit files and compute from those, together with the observation site's position a predicted range. For validation purposes the difference between the observed and the predicted range is investigated.

Thorough testing was conducted with the kinematic orbits of GRACE and Swarm mission satellites which established by Dr. Zehentner within the scope of his doctoral thesis. Additionally, results where compared to results from TU Delft and the Astronomical Institute at the University of Bern.

Acknowledgment

At this point I want to thank all the people who supported me with the work on this thesis in one way or another. This includes, first of all, my supervisor Torsten Mayer-Gürr for offering me to work on this topic and his unconditional and immediate help and support at any time.

I also want to thank Norbert Zehentner who provided me with some of the material, which was necessary for this work and also with helpful advices.

I am very grateful to my colleagues, friends and family who always supported me in all my endeavours. To all of you I say: Thank you!

Contents

List of Figures

List of Tables

Chapter 1

Introduction

1.1 Motivation

Several space techniques exist for geodetical purposes. This variety of techniques allows for validation and canceling out systematic errors of a specific system. Very Long Baseline Interferometry (VLBI) uses the signal emitted by very distant astronomical radio sources, which arrives at different times for spatially separated observation stations on Earth. Doppler-effect based systems like the French Doppler Orbitography and Radiopositioning Integrated by Satellite (DORIS) system rely on ground based radio beacons which are received and interpreted by dedicated passing satellites. The most prominent ones are the Global Navigation Satellite Systems (GNSS) with the representatives Global Positioning System (GPS), Global Navigation Satellite System (GLONASS) and Galileo. These systems work on radio transmitted time signals transmitted from multiple satellite to precisely determine positions on Earth. The last technique is referred to by Satellite Laser Ranging (SLR) and is the technique investigated within this thesis. This technique relies on range determination by the two way travel time of a laser pulse transmitted to a reflector on a satellite. There have also been reflectors set up on the surface of the Moon. The observation of these is referred to by Lunar Laser Ranging (LLR).

The advantage of SLR is that it is completely independent of other measurement systems and therefore offers a perfect validation tool. Many observation sites are spread all over the globe, constantly producing a huge number of observations which a available for free from dedicated data centers. Several software projects already exist for the analysis of those observations. Representatives of these are the GEODYN-II software [Pavlis et al., 1999] by NASA or the SATellite ANalysis (SATAN) software [Sinclair, 1986] developed by the Royal Greenwich Observatory, Herstmonceux. Because error modeling is becoming more and more sophisticated and new possible applications emerge those such software projects undergo constant development in order to push the achievable accuracies further and further.

At the current state accuracies in the range of a few centimeters are feasible with new developments like systems with two different laser wave lengths trying to push the accuracy to the millimeter level.

1.2 Goals and thesis outline

The Theoretical Geodesy and Satellite Geodesy working group at Institute of Geodesy (IfG) at Graz Technical University develops and maintains a comprehensive software project, referred to by GROOPS, which offers tools for a variety of geodetic tasks. The aim of the thesis is to extend this existing software by a tool capable of reading SLR observations and comparing them to expected results calculated from given satellite orbits. This also involved implementation of various error models to cope with the errors present at laser ranging measurements.

The finished implementation was tested and verified by investigating the orbits of the GRACE and Swarm missions, which have been determined by Dr. Zehentner within the scope of his doctoral thesis [Zehentner, 2017] at Graz University of Technology. In [Zehentner, 2017] the mean Root Mean Square (RMS) values of the GRACE satellite orbits have been determined to be in the range of about 3 cm and the mean RMS values of the Swarm satellite orbits at about 3-4 cm. For this validation process the software package developed by Harald Wirnsberger [Wirnsberger et al., 2014] at Institut für Weltraumforschung (IWF) at the Austrian Academy of Sciences. Thus, the aim was achieve comparable with accuracies with the newly developed software.

The thesis is divided into seven chapters. Chapter 2 provides some of the theoretical fundamentals while chapter 3 briefly introduces the satellite missions (GRACE and Swarm) whose orbits were investigated within the scope of this thesis. In chapter 4 the principles of Satellite Laser Ranging are presented in detail together with some historical background. Yet, the focus lies on the various necessary correction terms; especially refraction correction. Chapter 5 refers to the actual implementation and test setup while chapter 6 visually presents and describes the obtained results. In the final chapter, chapter 7, the results are interpreted and compared to the expectations before a brief outlook is presented.

Chapter 2

Theoretical Fundamentals

This chapter briefly describes most of the underlying mathematical and physical concepts which are needed in the following chapters.

Various reference frames as well as their intended purposes will be explained. Section 2.3 deals with the role of time in satellite geodesy and introduces the most important timing scales for scientific application. Sections 2.4 and 2.5 provide some insight into Precise Orbit Determination and data compression in form of Normal Point data.

2.1 Reference Frames

For geodetic observations and applications precise reference frames are required for interpreting and processing of measurements. With observation techniques becoming more and more accurate reference frames are required to become more and more accurate as well. Thus, they undergo constant development with new instances emerging every few years.

There is an important distinction between the terms *Reference System* and *Reference Frame*. A reference system is thereby the thorough conceptual definition with the definition of an origin and three axis. The reference frame is the practical realization, realized through observations [Seeber, 2003, p.12][Hofmann-Wellenhof et al., 2003].

When observing the movements of satellites or celestial bodies it quickly becomes obvious that at least two reference systems are required for it is hard to describe the movement of satellites in an Earth fixed system, rotating with the Earth. Vice versa it is not applicable to handle positions on the Earth's surface in a space fixed system because of the constant changing of coordinates due to the Earth's rotation. To overcome this problem Earth fixed *Terrestrial Reference Systems* (TRSs), for Earth-based observations, and space fixed *Celestial Reference Systems* (CRSs) for satellite and celestial body motion have been defined.

Furthermore *Local-level Systems* with their origin on the Earth's surface have been defined for navigational purposes and *Body Systems* to describe the accelerations and forces acting on a vehicle.

In addition to the reference systems themselves a precise knowledge of their relations to each other is required in order to define the transformation from one to another.

2.1.1 Celestial Reference Frames

Reference systems tend to be defined in a way that they are either not moving at all or move in a constant rectilinear motion. This is a necessary prerequisite for Newton's laws of motion to be valid within the system. Such systems are referred to as *Inertial Systems*. However, the origin of a CRS, which is defined either as the Earth's center of mass or the center of mass of the Solar System, experiences tiny accelerations. Hence the respective systems are said to be *quasi-inertial*.

Differing on their placement of origin two CRSs have been defined, denoted *Barycentric Celestial Reference System* (BCRS), if the origin coincides with the barycenter of the solar system, and *Geocentric Celestial Reference System* (GCRS), if the origin is at the Earth's geocenter. For the description of the motion of near-Earth satellites the latter is advantageous.

The x-axis is defined such that it points to the vernal equinox (VE). The z-axis is orthogonal to the orbital plane or coincides with the Earth's rotation axis and the y-axis is perpendicular to the others in order to form a right-handed system.

The realization of a CRS, a Celestial Reference Frame (CRF), is conducted by Very Long Baseline Interferometry (VLBI) measurement to extremely far away "fixed" objects. Such objects exist in the form of so called *Quasars* which are very distant and bright cluster of stars. An important CRF is the *International Celestial Reference Frame* (ICRF) provided by the *International Earth Rotation and Reference Systems Service* (IERS). The second iteration of this reference frame was released in 2009 and is constructed with 3414[1] extragalactic radio sources [Seeber, 2003, p.10-14] [Mansfeld, 2013, p.32].

2.1.2 Terrestrial Reference Frames

A TRS is beneficial for terrestrial navigation and describing the positions of observation stations. It is defined with the origin at the Earth's center of mass, the z-axis pointing into the direction of the mean polar axis, the x-axis pointing through the zero longitude at the equator (the longitude running through Greenwich) and the y-axis perpendicular to the two previously defined. The geocenter and the orientation of the rotation axis are not directly obtainable through observations, but an ideal system has to be approximated.

For scientific use the realization of the TRS by IERS, the *International Terrestrial Reference Frame* (ITRF) is used. It is created by incorporating several independent geodetic techniques including Doppler, GNSS, SLR and VLIBI to reduce systematic errors in the overall result. Every few years a new realization is released with the year of the most recent contributing data as postfix in the name (e.g. ITRF2005, ITRF2008, ITRF2014) [Seeber, 2003, p.15-16].

2.1.3 Local-level Frame

The local-level frame is a reference frame whose origin can be located at an arbitrary position on the Earth's surface. It is only applicable over a rather small region where the Earth's curvature does not play a dominant role.

The system's x-axis points towards the North, its y-axis towards the East and its z-axis perpendicular to the previous two; either towards the local zenith (yielding a left-hand

[1] `https://www.iers.org/IERS/EN/DataProducts/ICRF/ICRF2/icrf2.html`

frame) or towards the nadir (yielding a right-hand frame) [Hofmann-Wellenhof et al., 2003, p.21-22]. Thus, it is often referred to as North-East-Up (NEU) system. Alternatively, there also exists a right-handed South-east-up system.

When it comes to transformation, it must be considered that the z-axis does not point towards the Earth's geocenter due to the non-spherical shape of the Earth [Jekeli, 2012, p.6].

2.1.4 Body Frame

The body frame is a three-dimensional Cartesian frame, which is usually closely related to a moving object like a satellite. Thus, the origin is defined such a way that it coincides in some way with the geometry of the object. In many cases it is located at the center of mass (CoM). The three axes should also be defined in a reasonable manner with respect to the object. E.g. for an aircraft the x-axis should correspond with the orientation of the fuselage, the y-axis with the orientation of the wings and the z-axis perpendicular [Hofmann-Wellenhof et al., 2003, p.23].

2.1.5 Transformation between Frames

The transformation of a point x in a arbitrary frame a, denoted x^a, to x^b in another arbitrary frame b can be achieved by a rotation matrix $\mathbf{R}$ with

$$x^b = \mathbf{R}_a^b x^a, \tag{2.1}$$

where $\mathbf{R}_a^b$ is referred to as "rotation from a to b". For Cartesian frames any rotation transformation can be achieved by not more than three consecutive rotations in reverse order

$$R_a^b = R_3(\alpha_3)R_2(\alpha_2)R_1(\alpha_1), \tag{2.2}$$

each describing the rotation around one of the axes. Those elemental rotation matrices are given by [Hofmann-Wellenhof et al., 2003, p.25] with

$$\mathbf{R_1}(\alpha) = \begin{bmatrix} 1 & 0 & 0 \\ 0 & \cos(\alpha) & \sin(\alpha) \\ 0 & -\sin(\alpha) & \cos(\alpha) \end{bmatrix}, \tag{2.3}$$

$$\mathbf{R_2}(\alpha) = \begin{bmatrix} \cos(\alpha) & 0 & -\sin(\alpha) \\ 0 & 1 & 0 \\ \sin(\alpha) & 0 & \cos(\alpha) \end{bmatrix} \quad \text{and} \tag{2.4}$$

$$\mathbf{R_3}(\alpha) = \begin{bmatrix} \cos(\alpha) & \sin(\alpha) & 0 \\ -\sin(\alpha) & \cos(\alpha) & 0 \\ 0 & 0 & 1 \end{bmatrix}. \tag{2.5}$$

2.1.6 Transformation between CRF and TRF

Overall, the difference between a Celestial Reference Frame and a Terrestrial Reference Frame is the Earth rotation. However, since the rotation axis is not fixed but moves with respect to an inertial system due to gravitational attraction of the Earth to other celestial bodies. This movement also needs to be considered in order to describe the

complete transformation. The additional motions are *Precession*, *Nutation* and polar motion [Seeber, 2003, p.14-17].

The precession is the secular component with a period of 26000 years is responsible for the rotation axis moving in a circle around the ecliptic pole. There is a rather constant inclination angle ϵ (*obliquity of the ecliptic*) of about 23 degrees between those two [Seeber, 2003, p.14-17].

The nutation is the periodic component of the motion of the rotation axis and has a period of about 18.6 years. It has a much smaller impact than the precession and is given by a component in obliquity $\Delta\epsilon$ and a component along the longitude $\Delta\psi$. They can be modeled by an expansion series with 263 coefficients given in the IERS conventions [Petit and Luzum, 2010].

In contrast to the precession and nutation the Earth rotation cannot be fully described by models, but has to be determined by daily observations. The IERS is responsible for measuring this rotation which is done using VLBI observations to distant radio sources [Seeber, 2003, p.14-17].

The overall transformation from TRF to CRF $\mathbf{R}_{TRF}^{CRF}(t)$ can thus be described as a series of rotations as

$$\mathbf{R}_{\mathbf{TRF}}^{\mathbf{CRF}}(\mathbf{t}) = \mathbf{N}(t)\mathbf{P}(t)\mathbf{R}(t)\mathbf{W}(t) \ , \tag{2.6}$$

with $\mathbf{N}(t)$ as the nutation, $\mathbf{P}(t)$ as the precession, $\mathbf{R}(t)$ as the Earth rotation and $\mathbf{W}(t)$ as the polar motion [Seeber, 2003, p.14-17]

2.2 Station Displacement

The Earth's surface experiences constant deformation. One of those is caused by gravitational attraction to the Sun and Moon, referred to by Earth tides. Due to the elastic characteristics of the Earth, a tidal bulge forms in the direction facing the Moon and also at the exact opposite side of the Earth's surface. The effects of tidal forces are strong enough to cause a lifting of the crust by about 0.5 meters [Melchior, 1974, p.275]. Observable patterns are related to the Earth's rotation.

The tides caused by gravitational attraction to the Moon feature a period of 12 hours, which corresponds to two tides a day and is also referred to by *semidiurnal*. Two consecutive tides are thereby not equal but have alternating *lower high* tides and *higher high* tides. The attraction to the Sun also generates tides, but those are much smaller in amplitude [House, 1995].

Conventional models for the displacement of positions on the crust incorporate body tides as a result from external tide generating potential and displacements resulting from ocean tidal loading and atmospheric pressure loading. Another effect is the rotational deformation due to polar motion which is not resulting from tidal attraction to other bodies but needs also to be taken into account.

2.2.1 Solid Earth tides

Tidal deformation of the solid Earth is modeled by means of the Love number h_{nm} and Shida number l_{nm} which account for the elasticity of the Earth. The IERS conventions [Petit and Luzum, 2010, p.100] provide equations for the displacement vector $\Delta\vec{r}_f$ for a tidal frequency f. There are different models for different period times, which are

$$\begin{aligned}\Delta\vec{r}_f = \sqrt{\frac{5}{4\pi}}H_f\Bigg\{ &\left[h(\phi)\left(\frac{3}{2}\sin^2(\phi)-\frac{1}{2}\right)+\sqrt{\frac{4\pi}{5}}h'\right]\cos(\theta_f)\hat{r} \\ &+ 3l(\phi)\sin(\phi)\cos(\phi)\cos(\theta_f)\hat{n} \\ &+ \cos(\phi)\left[3l^{(1)}\sin^2(\phi)-\sqrt{\frac{4\pi}{5}}l'\right]\sin(\theta_f)\hat{e}\Bigg\}\end{aligned} \tag{2.7}$$

for long-period tides

$$\begin{aligned}\Delta\vec{r}_f = -\sqrt{\frac{5}{24\pi}}H_f\Bigg\{ &h(\phi)3\sin(\phi)\cos(\phi)\sin(\theta_f+\lambda)\hat{r} \\ &+\left[3l(\phi)\cos(2\phi)-3l^{(1)}\sin^2(\phi)+\sqrt{24\pi}5l'\right]\sin(\theta_f+\lambda)\hat{n} \\ &+\left[\left(3l(\phi)-\sqrt{\frac{24\pi}{5}}l'\right)\sin(\phi)-3l^{(1)}\sin(\phi)\cos(2\phi)\right]\cos(\theta_f+\lambda)\hat{e}\Bigg\}\end{aligned} \tag{2.8}$$

for dirunal tides and

$$\begin{aligned}\Delta\vec{r}_f = \sqrt{\frac{5}{96\pi}}H_f\Bigg\{ &h(\phi)3\cos^2(\phi)\cos(\theta_f+2\lambda)\hat{r} \\ &-6\sin(\phi)\cos(\phi)\left[l(\phi)+l^{(1)}\right]\cos(\theta_f+2\lambda)\hat{n} \\ &-6\cos(\phi)\left[l(\phi)+l^{(1)}\sin^2(\phi)\right]\sin(\theta_f+2\lambda)\hat{e}\Bigg\}\end{aligned} \tag{2.9}$$

for semidiurnal tides. $h^{(0)}$, $l^{(0)}$, $h^{(2)}$, h', $l^{(1)}$, $l^{(2)}$, l' are representations of the Love and Shida numbers given by Mathews et al. in [Mathews et al., 1995]. $h(\phi)$ and $l(\phi)$ are defined as

$$h(\phi) = h^{(0)} + h^{(2)}(3\sin^2(\phi)-1)/2 \text{ and} \tag{2.10}$$

$$l(\phi) = l^{(0)} + l^{(2)}(3\sin^2(\phi)-1)/2\ . \tag{2.11}$$

H_f is the amplitude of the tide of frequency f, ϕ and λ are the latitude and longitude of the station, θ is the tidal argument of constituent of frequency f and $\hat{r}$, $\hat{e}$ and $\hat{n}$ are the normal vectors in radial-, eastern- and northern direction respectively.

2.2.2 Ocean tides

The fluid ocean mass is also affected by tidal attraction, causing time-varying deformations of the crust with a magnitude of up to 100 mm. The center of mass of the fluid masses periodically shifts resulting in a counter-motion of the center of mass of the solid Earth. Observation stations which are tied to the solid Earth have to consider this motion.

Since the motion of ocean masses is strongly dependent on regional conditions an global representation by means of analytical expressions is not convenient. Thus, formulations

for individual grids are established. In IERS conventions [Petit and Luzum, 2010] the displacement component Δc of a particular site at time t is given by

$$\Delta c = \sum_j A_{cj} \cos(\chi_j(t) - \phi_{cj}), \tag{2.12}$$

with the amplitude A_{cj} and phase ϕ_{cj} describing the loading response for the chosen site and $\chi_j(t)$ as the astronomical argument. A_{cj} and ϕ_{cj} for a given site is provided by the ocean loading service[2]. Conventionally a discrete set of harmonics from the "long-periods" as well as diurnal and semidiurnal ones are considered [Petit and Luzum, 2010].

2.2.3 Atmospheric pressure loading

Surface pressure oscillations are caused by diurnal heating of the atmosphere. They feature diurnal, semidiurnal and higher harmonics. The amplitudes of the deformation of the crust are in the range of the amplitudes caused by ocean tides effects in vertical direction. In horizontal direction they are smaller by a factor of 10. To calculate station displacement on the Earth's surface IERS conventions [Petit and Luzum, 2010] recommend the application of the model by Ray and Ponte [Ray and Ponte, 2003], which accounts for diurnal and semidiurnal effects.

2.2.4 Pole Tides

The Earth's rotation axis is not fixed but is slightly shifting within a square of about 20 meters causing elastic responses of the Earth's crust. With station displacements in the range of a few centimeters this effect has to be taken into account for precise measurements [Petit and Luzum, 2010].

In IERS conventions [Petit and Luzum, 2010] the changes of Cartesian coordinates dX, dY and dZ in a TRS is given by

$$[dX, dY, dZ]^T = R^T [S_\theta, S_\lambda, S_r]^T, \tag{2.13}$$

with rotation matrix R, the horizontal displacements S_θ and S_λ, and the radial displacement S_r. The individual displacement terms are functions of the first order perturbation in the potential ΔV given by [Wahr, 1985].

2.3 Time

Time scales are essential in order to provide observations and positions with a clearly distinguishable epoch. The definition of a time scale is thereby not trivial and constant advancements in time measurement lead the way to new concepts and definitions.

The first time scales were based on the duration until the same spot on the Earth's surface faces the Sun again, which is traditionally given with 86 400 seconds per revolution and referred to as *solar day*. Another method measures the time of a rotation with respect to the starry sky. This is denoted *sidereal day* and it is about 4 minutes short of the solar day.

[2] `http://froste.oso.chalmers.se/loading`

With the development of sophisticated atom clocks a whole new group of time scales emerged in the 1960s - the time scales based on atomic clocks. Scales from this group are the most important for geodetic application and include *Atomic Time*, *GPS Time* and *Universal Time Coordinated* (UTC).

None of these time scales have taken into account relativistic effects. Thus, time scales accounting for these like *Geocentric Coordinate Time* (TCG) or *Barycentric Coordinate Time* (TCB) have been established [Montenbruck and Gill, 2012, p.157-159].

In real life there is always some deviation between a conceptual definition of time and the actual realization. In oder to improve precession it should be attempted to keep this deviation as small as possible. Also the deviation between different time scales shall be modeled with highest possible accuracy.

2.3.1 Atomic Time

The atomic time, also referred to as *Temps Atonomique International* (TAI), is a time scale purely based on atomic clocks. It also became the SI-definition of time with 1 second equaling the 9 192 631 770 periods of a low-energy state transition of a Cesium 133 atom. Today also Hydrogen and Rubidium based atom clocks are used with Cesium based systems offering the best long term stability.

The TAI is the weighted mean of many separate clocks. About 45 institutions around the world compare and synchronize their atomic clocks on a regular basis [Mansfeld, 2013, p.39].

2.3.2 GPS Time

The GPS time is the time scaled used by the Global Positioning System (GPS). Like TAI it is a time scale based purely on atomic time, but completely independent from TAI. It started with zero on 6th January 1980 and is now several seconds ahead of UTC due to the lack of leap seconds which are not present in GPS time [Mansfeld, 2013, p.39].

2.3.3 UTC

Atomic time is highly uniform while the UT1/GMT time scale (c.f. section 2.3.4) is highly adapted to the Earth's rotation. The *Universal Time Coordinated* (UTC) can be seen as a compromise between UT1 and Atomic time. Hence, it differs from TAI by an integer amount of seconds so that it is as close as possible to UT1. This relation is given by

$$UTC = TAI - n, \;\; n \in \mathtt{N} \; . \tag{2.14}$$

The n are the so called leap seconds. Their amount can be changed on 1st January or 1st July of the year in order to keep the deviation between UT1 and UTC below an absolute value of 0.7 seconds

$$UTC - UT1 \overset{!}{\leq} 0.7s. \tag{2.15}$$

The occurrence of leap seconds cannot be predicted but is a conclusion from constant observation of the Earth's rotation speed. In 1992 the difference of UTC and UT1 was already 8 seconds due to leap seconds [Seeber, 2003, p.31].

2.3.4 UT1/GMT

The *Universal Time 1* (UT1) also known as *Greenwich Mean Time* (GMT) is directly related to the rotation of the Earth. The "mean" in the name is due to a fictional "mean Sun" which is a substitute for the true Sun, for the true Sun experiences quite strong variations of the hour angle during the year. It is thus not suitable for a rather uniform time scale.

2.4 Precise Orbit Determination

Precise orbit determination (POD) refers to the determination of the orbit of an artificial satellite with the highest possible accuracy. While there is no distinct threshold accuracy to be met in order to be qualified as POD, it can be assumed that everything was done for the specific determination method to achieve the best possible accuracy. It can be distinguished between three major types of POD, including:

- dynamic orbit,
- reduced-dynamic orbit and
- kinematic orbit.

2.4.1 Dynamic orbits

Dynamic orbit determination relies on modeling the forces, which act upon a satellite. This involves atmospheric drag, solar radiation pressure, gravitational forces and others. Together with the satellite's mass the accelerations over time can be expressed mathematically. Integrating those twice over the time yields the trajectory with two constant vectors resulting from the integrations. Those refer to the initial velocity as well as the initial position and are referred to as *epoch state*. They can be estimated by as least-square fit of the calculated trajectory to the observed one. The precession of the solution depends heavily on the quality of the applied force models. Hence, the solution can be further improved by adjusting the parameters of the force models [Yunck, 1992] [Zehentner, 2017].

The advantage of this type of POD is that no continuous tracking of the satellite is required.

2.4.2 Reduced-dynamic orbits

The reduced-dynamic orbit type combines the advantages of dynamic and kinematic orbits. Deficiencies in the dynamic force models which accumulate over time are counteracted with empirically obtained accelerations. The amplitudes are estimated as part of the orbit determination and are assumed to be constant within a defined interval [Montenbruck et al., 2005].

2.4.3 Kinematic Orbits

By definition "kinematic" deals with the motion of a point without consideration what causes this motion. Thus, the approach of kinematic orbit determination relies purely

on three-dimensional observations. For an accurate orbit estimation a huge number of observations is required. This is the reason why kinematic orbit solutions are mostly determined by GNSS observations which allow for a continuous three-dimensional tracking of satellites with a sufficiently high precision [Yunck, 1992] [Zehentner, 2017].

However, there is also the possibility of combined solutions, e.g. GPS/SLR POD, as discussed in [Svehla and Rothacher, 2003].

GNSS apply not just pseudoranges but also carrier-phase measurements for precise orbit determinations. This results in an ambiguity by an integer multiple of one cycle. In a first step the ambiguities are fixed to a float number with least-square techniques. Such solutions are referred to as *kinematic float*. Since the "real" solution is of integer type there exist various methods, like double-differenced GPS [Laurichesse et al., 2009], to find the integer solution which is related to the float solution. This type of solution is in the following referred to by *kinematic fixed*.

2.5 Normal Point Data

Since a SLR site conducts up to several thousand measurements on a single satellite pass, the gathered data needs to be compressed in a well defined manner in order to allow for convenient data exchange and analysis. Furthermore the raw observations feature a high correlation and observation noise which should be reduced as much as possible.

The general concept is to remove outliers from the observations and to define so called normal points (NP), which are representative for a series of measurements. According to Seeber [Seeber, 2003, p.370] the most commonly used method for creating normal point data is the multi-step procedure recommended at "Herstmonceux Laser Workshop". The first step consists of subtracting the raw observed ranges d_0 by a series of predicted ranges d_p in order to obtain a set of residuals d_r with

$$d_r = d_0 - d_p \ . \tag{2.16}$$

The predicted ranges d_p can thereby be obtained by any arbitrary method, e.g. polynomial prediction models of the observed orbit. After that, great outliers are removed from the observations.

A polynomial $f(p)$ is fitted to the remaining observations and the resulting residuals f_r are calculated with

$$f_r = d_0 - f(p) \ . \tag{2.17}$$

From f_r, the measurements exceeding the mean σ by more than three times are removed and f_r is recomputed iteratively until the number of observations does not change no more.

In the next step the series of measurements is split up into equally sized intervals, denoted *bins*. The interval length of those bins is more or less a design decision. Examples of interval lengths given by [Seeber, 2003, p.371] include 2 minutes for the LAGEOS satellite and half a minute for STARLETTE.

The actual normal point is calculated by adding the mean value of all residuals of the interval f_r to the trend function at the center of the interval.

Chapter 3

Satellite Missions

This chapter briefly introduces the satellite missions, which have been of relevance for the work on this thesis. These include the Gravity Recovery and Climate Experiment (GRACE) and the Swarm mission.

3.1 Swarm Mission

Swarm is a satellite mission by ESA, consisting of a constellation of three identical satellites, dedicated to investigate the Earth's magnetic field. The mission was developed by ESA's research facility European Space Research and Technology Centre (ESTEC) in the Netherlands and launched on November 22, 2013 from Plesetsk Cosmodrome in northern Russia. After an initial commission phase of three months it is scheduled to have a lifetime of 4 years [Plank et al., 2013].

All three satellites initially operate on near-polar orbits. Two of them are almost side by side at an initial altitude of about 460 km and the third one at a (by 0.6 degrees) shifted inclination. The longitude of the ascending node of the orbit of this third satellite drifts, so that it intersects the orbit of the other two in an angle of 90 degrees after a mission time of three years. At the same time the altitude of the two lower satellite constantly decreases due to atmospheric drag phenomenons, which are more prominent at altitudes below 500 km. Until the end of the mission it will decrease to about 300 km above surface [Plank et al., 2013].

The identical satellites are of trapezoidal shape with a long boom as depicted in figure 3.1. The boom serves as a platform for the magnetometer, which is mounted at the end of it in order to avoid magnetic interference from the satellite itself as good as possible. The 9 meter long slim shape has a front face of only 1 m^2 in total area, to minimize the effects of atmospheric drag. Apart from the boom, which is deployed during the first days in space, the satellite has no moving parts which could interfere with measurements. Besides magnetometers, electric field sensors, accelerometers and GPS receivers, the satellite is equipped with a laser retro reflector from GFZ Research Centre for Geoscience Potsdam, Germany, which is described in section 4.7 [Plank et al., 2013].

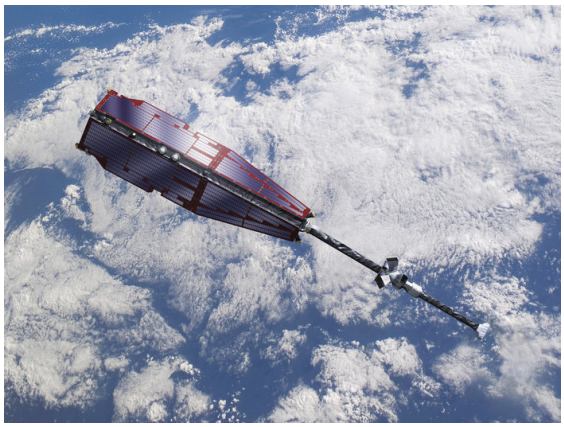

Figure 3.1: Artist's view of Swarm ©ESA-P. Carril, 2013[1].

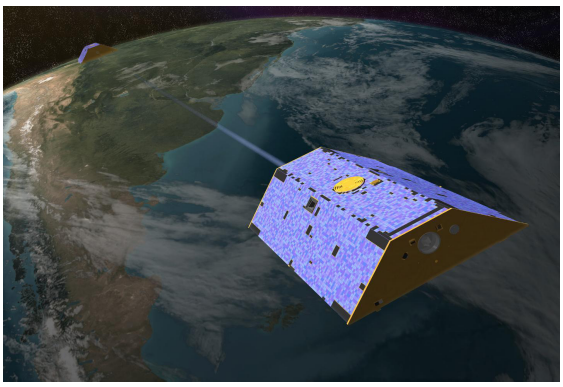

Figure 3.2: Artist's concept of Gravity Recovery and Climate Experiment ©NASA/JPL-Caltech[2].

3.2 GRACE Mission

The GRACE mission was a joint project by NASA and DLR consisting of two identical satellites in the same orbit. The mission was launched on March 17, 2002 and it was intended for a lifespan of 5 years. In a near-circular polar orbit with an inclination of 89.5 degrees the satellites are separated by a distance of 220 km along track as depicted in figure 3.2. The initial altitude of approximately 500 km decreases by 30 m per day [Tapley et al., 2004].

The goal of the project was to track changes in Earth's gravity field more accurately than preceding missions with a nominal spatial resolution of 400 km to 40 000 km and a temporal resolution of 30 days. With the satellites taking phase measurements of the same area in quick succession, oscillator instability can be removed in ground processing. Non-gravitational forces can also be removed by means of precise accelerometers [Tapley et al., 2004].

[2] http://www.esa.int/spaceinimages/Images/2013/11/Artist_s_view_of_Swarm9
[2] https://www.nasa.gov/mission_pages/Grace/multimedia/

Chapter 4

Satellite Laser Ranging

Satellite Laser Ranging is an observation technique belonging to the field of satellite geodesy, where the - in most cases - two-way travel time of a laser impulse sent from an observation site on ground to a satellite (equipped with a dedicated reflector) is used to determine the distance between the two.

The application of SLR as a means of distance determination emerged in the 60s with the first successful experiments conducted by a NASA team in the time between October 11, 1964 and November 13, 1964. In ten individual sessions the Beacon-B satellite was tracked with an accuracy in the range of 3 m [Xu, 2010, p.302] [Montenbruck and Gill, 2000, p.202]. This success led to the emerging of several SLR stations, dedicated geodetic satellites (e.g. Geodetic Earth Orbiting Satellite (GEOS-1) during the 70s) and a continuous research in the field of SLR, pushing the achievable accuracies further and further. With the success of the Apollo missions it was possible to place retro reflectors on the surface of the Moon, creating a whole new branch of SLR denoted Lunar Laser Ranging (LLR).

There are numerous fields of application for SLR. From early on it was used for the determination of the Earth's gravitation model, with GEOS-1 SLR measurements being already included into the Earth Gravitational Model 1996 (EGM96) [Xu, 2010, p.303]. Another field of application is the measurement of slow-varying geodynamical processes of the Earth like ocean- and body-tides, tidal friction, crustal motion, polar motion and Earth rotation. Furthermore, it can also be used to determine precise station- and satellite positions and calibrate GNSS systems [Seeber, 2003, p.359] [Montenbruck and Gill, 2000, p.203].

Yet, the observation technique does not come without drawbacks. The reliance on laser light makes it highly weather dependent. Thus, there is no operation possible on clouded skies. Furthermore, the ground sites come with high costs for establishing and maintenance. On the other hand, a huge advantage is that no active elements are required on the space segment and high accuracies are achievable [Seeber, 2003, p.356-357].

At the same time the basic principle is simple. A laser pulse is transmitted to a reflector array on a satellite where it is reflected back and received by a dedicated light detecting device. In order to hit the reflector on the satellite an optical telescope, co-aligned with the laser transmitter needs to precisely track the respective satellite. At the departure of the laser pulse a counter is started which is stopped upon receiving the reflected signal. Most observations are supported by human interaction to cope with issues like misalignment or

clock offsets, which need to be carefully documented and applied on the measurements during post-processing [Xu, 2010, p.304-305]. The recorded SLR measurements need to include at least

Satellite identification: This unambiguously identifies the satellite. Today scientific satellites are referred to by a 4 digit Satellite Identification Code (SIC) [Ricklefs, 2006].

Epoch: An observation needs to be tied to a specific epoch. The time of departure of the laser pulse is used with GPS time as time scale [Ricklefs, 2006].

Time of flight: The two-way time of flight of the laser impulse. Published records are usually already corrected by the systematic error of the observation site.

System specific details: Those include setup details like the wave length of the used laser or the calibrated system time delay.

Environmental conditions on site: The environmental conditions on site during the observation are necessary inputs for modeling the tropospheric delay and have to include at least surface pressure, temperature and humidity.

In 2009 version 1.01 of a new standard for ranging observations was published, denoted Consolidated Ranging Data (CRD) format [Ricklefs, 2006]. The format is capable of holding all the previously mentioned information in a flexible and extensible manner and is described more thoroughly in appendix A.4.

4.1 Observation Equation

The basic equation describing a two-way measurement is given by Seeber [Seeber, 2003, p.336] by

$$d = \frac{\Delta t}{2} c, \tag{4.1}$$

with d as the one-way distance, Δt as the measured time between emitting and receiving the laser pulse and c as the speed of light.

Due to various error sources and other influences in real world observations, equation 4.1 needs to be extended by various correction terms to cope with these effects, giving

$$d = \frac{1}{2} c\Delta t + \Delta d_0 + \Delta d_S + \Delta d_r + \Delta d_R + \eta, \tag{4.2}$$

where Δd_0 is the eccentricity correction on ground, Δd_S the eccentricity correction at the satellite, Δd_r the atmospheric refraction correction, Δd_R the relativistic range correction and η the culmination of all remaining observation errors, which are not yet described [Seeber, 2003, p.367]. An estimation of the typical magnitudes of the correction terms is referred to in table 4.1.

Table 4.1: Corrections with their expectable magnitudes and the variable by which they are referred to in equation 4.2.

Variable	Correction	Magnitude
Δd_r	Refraction Correction	2.4 m to more than 10 m
Δd_0	Station offset	Completely dependent on station setup
Δd_S	Array offset	up to several meters (dependent on satellite geometry)
Δd_S	CoM offset	in many cases zero if the CoM coincides with the satellite's coordinate origin
Δd_S	LRR incident dependent	4 ± 2 mm (for reflector hardware described in section 4.7)
Δd_R	Relativistic range correction	In the range of a few millimeters[1]

[1] Source [Xu, 2010, p.316]

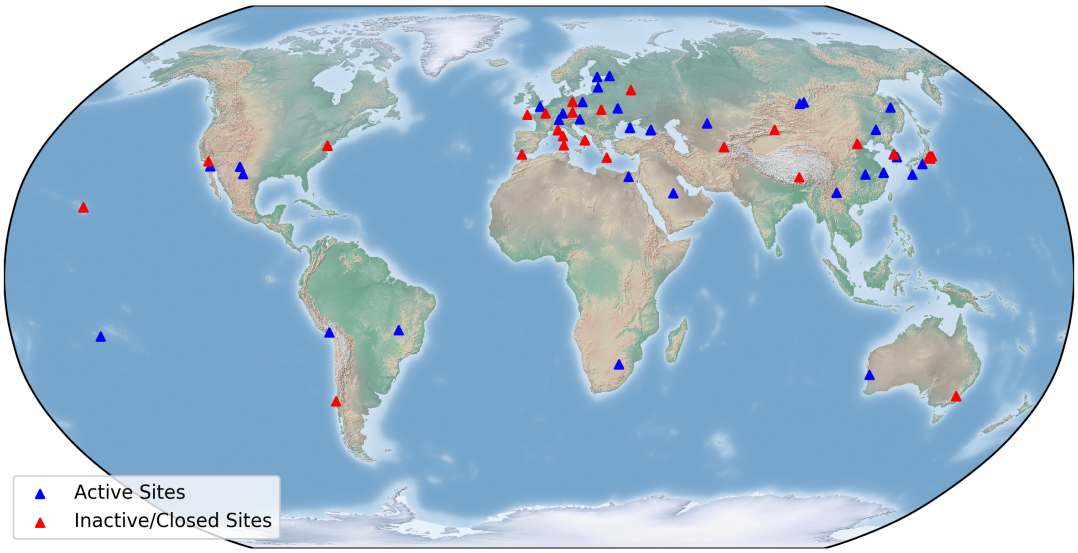

Figure 4.1: Worldwide distribution of SLR observation sites in 2018.

4.2 Ground Stations

As in 2018 there exists a total of 45 currently active SLR observation sites with 7 more scheduled to be ready until 2020[1]. Their global distribution is depicted in figure 4.1.

4.3 Eccentricity correction

While the satellite's position is given by the coordinate origin of the satellite's body-frame, the arriving laser impulse is not reflected there, but somewhere on the satellite's surface where the Laser Reflector Array (LRA) is mounted. Thus, a precise knowledge of the relation between those two points is necessary. Also, the LRA usually consists of multiple individual corner cube retroreflectors (CCR) facing in different directions and in most cases the laser pulse gets reflected by more than one of those. The returning pulse at the SLR cite is thus the combination of all single returns. A sent pulse of about 200 ps can become about twice the length due to the arrival at different CCRs at slightly different times [Xu, 2010, p.311]. This phenomenon is referred to as *laser jitter* [Seeber, 2003, p.370].

While the offset of the LRA Phase Center from the satellite's coordinate origin can be determined with high accuracy for spherical satellites, it is more complex for satellites of other geometries [Seeber, 2003]. The ILRS maintains on its website a tabular description of the LRA array offsets[2] for active satellite missions. Note that the LRA position is thereby not given relative to the satellite's coordinate origin but it's Center of Mass (CoM). In many cases the CoM coincides with the satellite's coordinate origin but there are also such cases where the position differs. In satellites equipped with propellant, the position of the CoM changes over time as more and more propellant is used up, leading to a different overall mass distribution.

The offset of the LRA Phase Center from the satellite's coordinate origin can thus be calculated, as depicted in figure 4.2 by superimpose the the CoM offset (represented by the green arrow) with the LRA offset from the CoM (represented by the red arrow). For the Swarm and GRACE mission satellites those offsets are given in table 4.2.

4.4 Station Range and Time Bias

The term *station bias* is ambiguous. There is a wide range of error terms, which are assigned to the station range and time bias by different sources. They include the non-linearities in the timer measuring the time of flight of the laser pulse, inaccuracies in the environmental sensors at the site, leading to errors in the tropospheric delay modeling, system delay and errors in the relation of the station's coordinate reference point and the SLR telescope reference point [Xu, 2010, p313-314].

Generally, the station biases can be classified as range- or time biases, where a positive range bias means that the measured range is too long and has to be subtracted by the range bias. Similarly, the time bias means that the epoch for which the observation was

[1] `https://ilrs.cddis.eosdis.nasa.gov/network/stations/index.html`

[2] `https://ilrs.cddis.eosdis.nasa.gov/missions/spacecraft_parameters/center_of_mass.html`

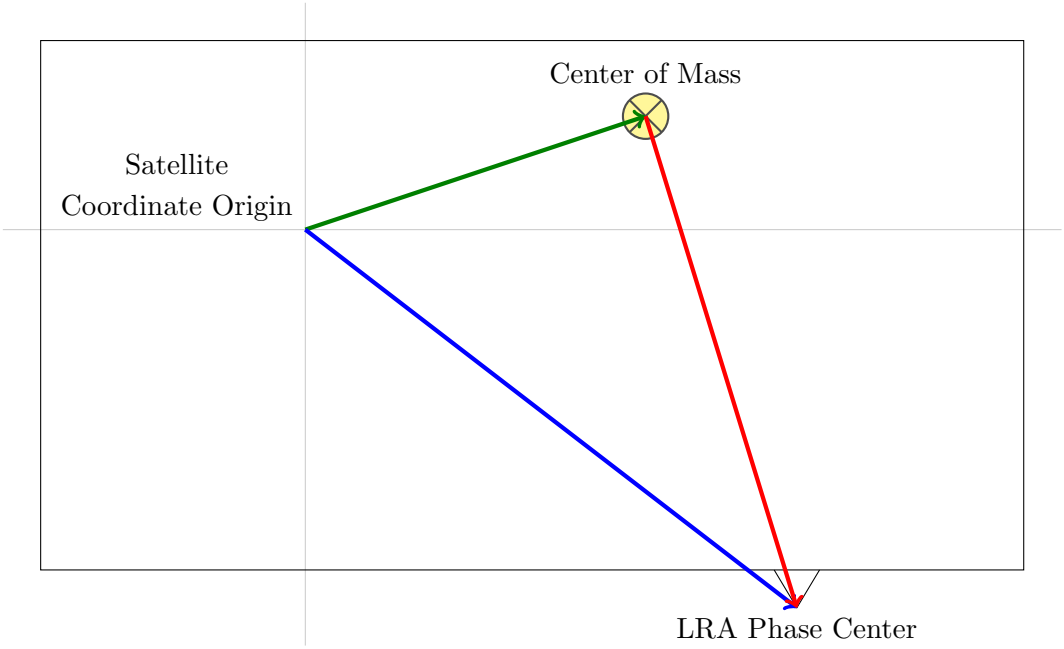

Figure 4.2: SLR Center of Mass Correction Concept as specified by ILRS[3].

Table 4.2: CoM offsets and LRA offsets for GRACE and Swarm satellites in satellite coordinates.

Satellite	**CoM Offset**			**LRA Offset (from CoM)**		
	x [mm]	**y [mm]**	**z [mm]**	**x [mm]**	**y [mm]**	**z [mm]**
Grace A[1]	0.00	0.00	0.00	-600.00	-327.50	217.80
Grace B[1]	0.00	0.00	0.00	-600.00	-327.50	217.80
Swam A[2]	-1910.11	0.00	-331.00	-2419.56	520.75	-31.05
Swam B[2]	-1969.84	-0.10	-330.96	-2419.56	521.73	-31.29
Swam C[2]	-1970.11	0.00	-331.04	-2420.10	521.12	-31.66

[1] Source: GRACE Laser Reflector User Manual [Grunwaldt et al., 2006].
[2] Source: Swarm Instrument Positions in Spacecraft Coordinates [Faust, 2013].

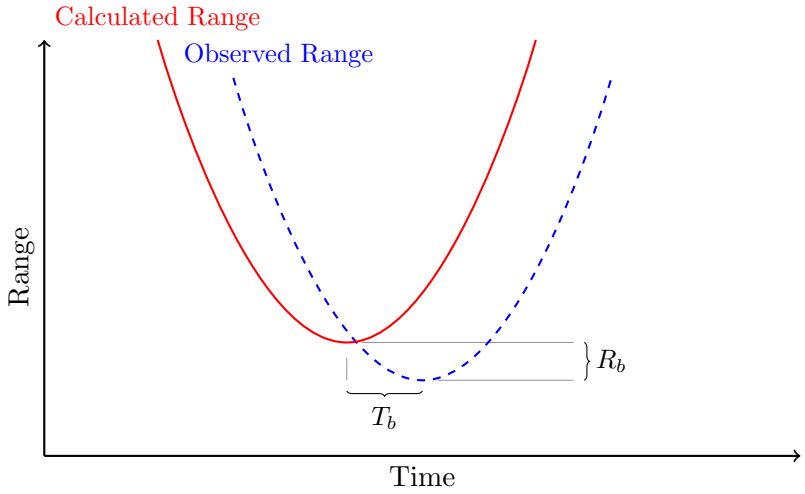

Figure 4.3: Concept of time and range bias estimation for SLR site. A satellite pass with an ascending- and a descending part is compared to an expected calculated trajectory. The differences in time and range of the two are estimated.

registered is too late. The time bias T_b is given by

$$T_b = UTC - T_{Site}, \tag{4.3}$$

where T_{Site} is the time at the site, containing a systematic calibrated timing error and an uncalibrated instrumental phase delay.

One of the challenges, when addressing these errors, is that range- and time biases are correlated and are usually not completely distinguishable. With enough NP measurements, distributed equally in all directions and over all elevations, the site's range- and time biases can be estimated by taking satellite passes with sufficient measurements (some SLR software packages require at least 8 NPs [Xu, 2010, p.316]) and compare the measurement over time and range to expected calculated ranges as depicted in figure 4.3. An ascending- and a descending component is required in order to achieve correct results. For determination of these two parameters either the averaged residuals can be taken or the curves can be fitted by high-degree polynomials which are compared to one another at their minima [Xu, 2010, p.315,p.316].

The system reference point (SRP) is also not perfectly aligned with the site's ITRF position with deviations being in the sub-millimeter range. Xu [Xu, 2010, p.314] states

> One can therefore assume that most, if not all, SLR stations have a small bias between the fixed to bedrock reference marker (the ITRF reference point) and the virtual SLR system reference point (eccentricity). Nevertheless, one also assumes that all effort was undertaken to determine these different distances and offsets as accurately as possible.

The eccentricity of the telescope reference point from the SRP, if not zero, also needs be taken into account. The telescope reference point is the point where the laser pulse is

[3] `https://ilrs.cddis.eosdis.nasa.gov/missions/spacecraft_parameters/CofMdiagramSLR.html`

emitted. The eccentricities are provided by the site's operator by means of North-East-Up correction terms in dedicated sites logs (cf. section A.1).

Obvious systematic errors also occur due to the fact that the laser pulse is not generated exactly at the SRP but at a known distance and transmitted there via mirrors [Seeber, 2003, p.360]. In general site operators should detect and remove any systematic errors to the millimeter accuracy.

4.5 Refraction correction

Refraction occurs due to the Earth's atmosphere. There are different approaches to split the atmosphere surrounding the Earth into layers but in terms of signal processing there are only two layers which are of interest. Those are the *troposphere* and the *ionosphere*.

The troposphere is the lowest layer and reaches up to a height of about 40 km. Even though it is narrow compared to the other layers it contains about 90 percent of the Earth atmosphere's mass and it is also the place where the majority of the weather takes place. In contrast the ionosphere the troposphere is inhabited by fairly neutral gases. Thus, signal processing in this layer depends mostly on water vapor and temperature, which are in turn dependent on height above the surface. The index of refraction is slightly above 1 at the surface and reaches towards 1 with increasing height [Seeber, 2003, p.368].

The location of the ionosphere is more vague, but it starts at around 70 to 100 km above surface and reaches upwards. This layer is filled with charged particles with night-day fluctuations affecting radio signals [Seeber, 2003, p.386]. For the wave lengths used by SLR systems the ionosphere does not noticeable affect the measurements. Thus, the overall refraction correction is also referred to as *tropospheric delay correction*.

In the observation equation 4.2 (where it is represented by Δd_r) it represents by far the most prominent correction term with correction values of about 2.4 meters in zenith direction. It increases quickly with dropping elevation angles to values of more than 10 meters for elevation angles below 15 degrees. The estimated corrections by different models for different elevation angles and a typical scenario is depicted are figure 4.4.

The calculation of the overall correction requires precise knowledge of the atmospheric parameters in the trespassed parts of the atmosphere. Apparently those parameters along the laser signal's path are unknown and have to be modeled as good as possible from the parameters measured at the SLR site during the observation.

The two models which are usually described and recommended in literature are the model by *Marini and Murray* [Marini and Murray Jr, 1973] and its successor by *Mendes et al.* [Mendes et al., 2002]. Other models include the approach by Saastamoinen [Saastamoinen, 1973] and Yan and Wang [Yan and Wang, 1999]. However, those do not offer any major advantage over the previously mentioned and IERS conventions recommends the use of the model by Mendes et al.

Recent development in refraction correction includes setups with two different laser light wave lengths, comparable to dual frequency systems in GNSS. This technology requires additional expensive hardware at the site and is still in experimental phase.

Due to the importance of atmospheric refraction correction for SLR measurement this is an area of ongoing research [Xu, 2010, p.308] [Seeber, 2003, p.368,p.369]. Mendes et al. [Mendes et al., 2002] describe it as "the main accuracy-limiting factor in modern space

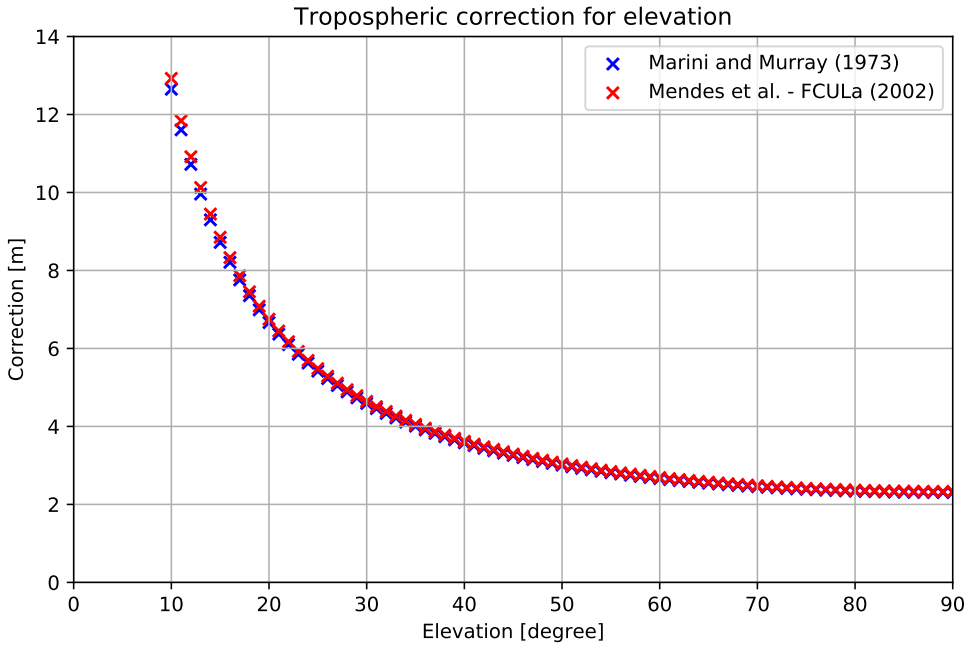

Figure 4.4: Estimated refraction correction of the models by Marini and Murray and Mendes et al. for the station located at Graz Lustbühel and ground temperature of 23^o C, surface pressure of 1013.24 hPa, relative humidity of 60%, and laser wave length of 532 nm. A strong increase for low elevation angles can be observed.

geodetic techniques."

4.5.1 Modell by *Marini* and *Murray*

The refraction correction by Marini and Murray [Marini and Murray Jr, 1973] was validated by ray-tracing to radiosondes. The correction Δd_r from equation 4.2 is given by

$$\Delta d_r = \frac{f(\lambda)}{f(\phi, H)} \cdot \frac{A + B}{\sin E + \frac{B/(A+B)}{\sin E + 0.01}}, \tag{4.4}$$

with

$$A = 0.002357 P_0 + 0.000141 e_0, \tag{4.5}$$

$$B = (1.084 \cdot 10^{-8}) P_0 T_0 K + (4.734 \cdot 10^{-8}) \frac{P_0^2}{T_0} \frac{2}{3 - 1/K}, \tag{4.6}$$

$$K = 1.163 - 0.00968 \cos(2\phi) - 0.00104 T_0 + 0.00001435 P_0, \tag{4.7}$$

E as the true elevation to the satellite in degrees, P_0 as the atmospheric pressure at the site in millibars, T_0 as the atmospheric temperature at the site in Kelvin, e_0 as the water vapor pressure at the site in millibars, λ as the wave length of the used laser in micrometers, ϕ as the latitude of the site in degrees and H as the geodetic height of the site in kilometers.

The water vapor pressure e_0 is usually not provided by the observation sites but it is proportional to the relative humidity R_h. With R_h in percent is given by

$$e_0 = \frac{R_h}{100} 6.11 \cdot 10^{\frac{7.5(T_0-273.15)}{237.3+(T_0-273.15)}}. \tag{4.8}$$

The laser wave length dependent term $f(\lambda)$ is given by

$$f(\lambda) = 0.9650 + \frac{0.0164}{\lambda^2} + \frac{0.000228}{\lambda^4} \tag{4.9}$$

and the term describing the influence of the station's location $f(\phi, H)$ is

$$f(\phi, H) = 1 - 0.0026\cos(2\phi) - 0.00031H \tag{4.10}$$

[Marini and Murray Jr, 1973][Seeber, 2003, p.368-369].

4.5.2 Model by *Mendes* et al.

In contrast to the model by Marini and Murray (cf. section 4.5.1) other tropospheric correction model divide the task of determining the overall correction value into two parts. Firstly, the determination of the delay in zenith direction, denoted zenith delay (ZD), and secondly the description of the influence of alternate elevation angles, referred to as mapping function (MF). This offers a huge advantage over the older, combined model by Marini and Murray because both parts can be developed, tested and combined independently [Mendes and Pavlis, 2004].

According to Mendes et al. [Mendes and Pavlis, 2004] the ZD d^z_{atm} can be split in a hydrostatic d^z_h and a non-hydrostatic component d^z_{nh} with

$$d^z_{atm} = d^z_h + d^z_{nh}. \tag{4.11}$$

The hydrostatic term is given by

$$d^z_h = 10^{-6} K^L_1 f_h(\lambda) Z_d R_d \int_{r_s}^{r_a} \rho dz, \tag{4.12}$$

where $K^L_1 = 0.8239568$ K Pa^{-1}, Z_d is the compressibility factor of dry air, ρ is the density of moist air, $R_d = 287.07153$ J kg^{-1} K^{-1} is the mean specific gas constant of dry air, r_s the geocentric radius of the SLR site, r_a the geocentric radius of the top of the neutral atmosphere and $f_h(\lambda)$ the dispersion equation for the hydrostatic component. The latter is given by

$$f_h(\lambda) = 10^{-2}\left[k^*_1 \frac{(k_0+\sigma^2)}{(k_0-\sigma^2)^2} + k^*_3 \frac{(k_2+\sigma^2)}{(k_2-\sigma^2)^2}\right] C_{CO_2}, \tag{4.13}$$

with $k_0 = 238.0185$ µm^{-2}, $k^*_1 = 19990.975$ µm^{-2}, $k_2 = 57.362$ µm^{-2}, $k^*_3 = 579.55174$ µm^{-2}. C_{CO_2} is defined by

$$C_{CO_2} = 1 + 0.53410^{-6}(x_c - 450), \tag{4.14}$$

with x_c as the carbon dioxide content and $\sigma = \lambda^{-1}$ as the inverse of the wave length. By filling in constants and further simplifications equation 4.12 can be rearranged to

$$d^z_h = 0.00002416579 \frac{f_h(\lambda)}{f(\varphi, H)} P_S, \tag{4.15}$$

where P_S is the surface barometric pressure in Pascal, and the location dependent term $f(\varphi, H)$ is

$$f(\varphi, H) = 1 - 0.00266\cos(2\varphi) - 0.00028H, \tag{4.16}$$

with the latitude of the station φ and the height of the station H in kilometers.

The non-hydrostatic component of equation 4.11 is given by

$$d^z_{nh} = 10^{-6}\left(K^L_2 f_{nh}(\lambda) - K^L_1 \varepsilon f_h(\lambda)\right)\int_{r_s}^{r_a}\frac{e}{T}dz, \tag{4.17}$$

with $K^L_2 = 0.7247600$ K Pa^{-1}, e as the water vapor pressure of moist air, T as the temperature and $\varepsilon = \frac{M_w}{M_d}$, with the molar mass of dry air M_d and the molar mass of wet air M_w. $f_{nh}(\lambda)$ is thereby the non-hydrostatic dispersion formula with

$$f_{nh}(\lambda) = 0.003101(\omega_0 + 3\omega_1\sigma^2 + 5\omega_2\sigma^4 + 7\omega_3\sigma^6) \tag{4.18}$$

and $\omega_0 = 295.235$, $\omega_1 = 2.6422$ µm^2, $\omega_2 = -0.032380$ µm^4 and $\omega_3 = 0.004028$ µm^6.

Similarly to equation 4.12, equation 4.17 can be simplified by filling in constants, giving

$$d^z_{nh} = 10^{-6}(5.316 f_{nh}(\lambda) - 3.759 f_h(\lambda))\frac{e_s}{f(\varphi, H)}, \tag{4.19}$$

with the surface water vapor pressure e_s.

4.5.3 Mapping Functions

The total atmospheric delay is commonly modeled by superimposing hydrostatic and wet components of the delay experienced in zenith direction (cf. equation 4.11). Each component is multiplied with a mapping function $m_h(\epsilon)$ and $m_w(\epsilon)$ respectively, modeling the delay with respect to the elevation angle ϵ [Mendes et al., 2002]:

$$d_{atm} = d^z_h m_h(\epsilon) + d^z_w m_w(\epsilon). \tag{4.20}$$

For wave lengths in the range of laser light the water vapor is negligible. Thus, equation 4.20 for the overall atmospheric range correction d_{atm} can be simplified to

$$d_{atm} = d^z_{atm} m(\epsilon). \tag{4.21}$$

There exist multiple MFs, but IERS conventions [Petit and Luzum, 2010] recommends the use of the FCUL mapping function developed by Mendes et al. [Mendes and Pavlis, 2004]. It is given by

$$m(\epsilon) = \frac{1 + \frac{a_1}{1+\frac{a_2}{1+a_3}}}{\sin(\epsilon) + \frac{a_1}{\sin(\epsilon)+\frac{a_2}{\sin(\epsilon)+a_3}}} \tag{4.22}$$

and has the form of a continuous fraction that equals 1 for an elevation angle ϵ of 90 degrees. The parameters a_i have been determined by conducting numerous ray tracing experiments at 180 individual, globally distributed stations through the year 1999. Radiosondes provided precise data on high altitude temperature, pressure and relative humidity. A total of 87 766 sets of coefficients have been determined in a least square approach from measurements of various different elevation angles and a laser wave length of

Table 4.3: Coefficients a_{ij} for the parameterizations FCULa and FCULb of the FCUL mapping function [Mendes et al., 2002].

a_{ij}	**FCULa**	**FCULb**
a_{10}	(12100.8 ± 1.9) 10^7	(11613.1 ± 1.6) 10^7
a_{11}	(1729.5 ± 4.3) 10^9	(-933.8 ± 9.7) 10^8
a_{12}	(319.1 ± 3.1) 10^7	(-595.8 ± 4.1) 10^{11}
a_{13}	(-1847.8 ± 6.5) 10^{11}	(-2462.7 ± 6.8) 10^{11}
a_{14}		(1286.4 ± 2.2) 10^7
a_{20}	(30496.5 ± 6.6) 10^7	(29815.1 ± 4.5) 10^7
a_{21}	(234.6 ± 1.5) 10^8	(-56.9 ± 2.7) 10^7
a_{22}	(-103.5 ± 1.1) 10^6	(-165.5 ± 1.1) 10^{10}
a_{23}	(-185.6 ± 2.2) 10^{10}	(-272.5 ± 1.9) 10^{10}
a_{24}		(302.0 ± 5.9) 10^7
a_{30}	(6877.7 ± 1.2) 10^5	(68183.9 ± 9.1) 10^6
a_{31}	(197.2 ± 2.8) 10^7	(93.5 ± 5.4) 10^6
a_{32}	(-345.8 ± 2.0) 10^5	(-239.4 ± 2.3) 10^9
a_{33}	(106.0 ± 4.2) 10^9	(30.4 ± 3.8) 10^9
a_{34}		(-230.8 ± 1.2) 10^5

532 nm. From those two different parameterisations have been retrieved, denoted FCULa and FCULb. FCULa is given by

$$a_i = a_{i0} + a_{i1} t_S + a_{i2} \cos(\varphi) + a_{i3} H, \;\; i = \{1, 2, 3\}, \tag{4.23}$$

with surface temperature t_S, φ as the station's latitude and H the station's orthometric height. FCULb is given by

$$\begin{aligned} a_i = a_{i0} + \left(a_{i1} + a_{i2}\varphi_d^2\right) \cos\left(\frac{2\pi}{365.25}(doy - 28)\right) \\ + a_{i3} H + a_{i4} \cos(\varphi), \;\; i = \{1, 2, 3, 4\}, \end{aligned} \tag{4.24}$$

with φ_d as the stations latitude in degrees and *doy* as the decimal number of UTC days since the beginning of the year. Coefficients a_{ij} for both parameterizations are given in table 4.3.

4.6 Systematic time delay

In Newtonian physics time passes uniformly and independent from location but Einstein's Theory of General Relativity showed that moving clocks tick slower than a non-moving clocks (time dilation). Although the errors resulting from relativistic effects are rather small compared to other error sources, they have to be taken into account when trying to reach millimeter accuracies.

The IERS conventions chapter 11 [Petit and Luzum, 2010, p.164] states

> In a reference system centered on an ensemble of masses, if an electromagnetic signal is emitted from x_1 at coordinate time t_1 and is received at x_2 at

coordinate time t_2, the coordinate time of propagation is given by

$$t_2 - t_1 = \frac{|\vec{x}_2(t_2) - \vec{x}_1(t_1)|}{c} + \sum_J \frac{2GM_J}{c^3} \ln\left(\frac{r_{J1} + r_{J2} + \rho}{r_{J1} + r_{J2} - \rho}\right), \tag{4.25}$$

where the sum is carried out over all bodies J with mass M_J centered at x_J and where $r_{J1} = |\vec{x}_1 - \vec{x}_J|$, $r_{J2} = |\vec{x}_2 - \vec{x}_J|$ and $\rho = |\vec{x}_2 - \vec{x}_1|$.

For near-Earth satellites all bodies apart from Earth can be omitted and equation 4.25 simplifies to

$$t_2 - t_1 = \frac{1}{c}\left[|\vec{x}_2(t_2) - \vec{x}_1(t_1)| + \sum_J \frac{2GM_E}{c^2} \ln\left(\frac{r_{E1} + r_{E2} + \rho}{r_{E1} + r_{E2} - \rho}\right)\right], \tag{4.26}$$

with G as the gravitational constant, M_E as the mass of the Earth, $r_{E1} = |\vec{x}_1 - \vec{x}_E|$, $r_{E2} = |\vec{x}_2 - \vec{x}_E|$ and $\vec{x}_E$ as the Earth's center. The distance ρ between transmitter and receiver is the observed distance without relativistic correction but after application of all other corrections.

According to Xu [Xu, 2010, p.316] this correction is in an area of 7 mm for the LAGEOS satellites which are at a mean altitude of 5 850 kilometers for LAGEOS-1 and 5 986 kilometers for LAGEOS-2[4].

4.7 Reflector Range Correction

The reflector geometry of the Laser Retro Reflector (LRR) mounted on the satellite's surface inflicts a small incident dependent error. Common satellite missions do not feature a single reflector but an array of reflectors. Thus, the returned signal is in most cases a culmination of multiple superimposed reflections.

This error and its correction is highly hardware dependent. The GRACE and the Swarm mission satellites which have been investigated for this thesis are equipped with the LRR manufactured by the GeoForschungs Zentrum at Potsdam, Germany. The same hardware is also deployed on the CHAMP, TerraSAR-X and TanDEM-X missions[5]. The reflector array consists of four prisms of fused quartz glass arranged on a regular 45 degrees pyramid as depicted in figure 4.6 [Neubert et al., 1998][Grunwaldt et al., 2006]. The technical specifications of the reflector is given in table 4.4. The cross point of the optical axis serves as reference point for the the cube corner prisms and is located outside the actual reflector geometry (cf. figure 4.5).

The range correction ΔR can be approximated by

$$\Delta R = (4 \pm 2) \text{ mm}, \tag{4.27}$$

or more accurately for the whole reflector array $\Delta\bar{R}$ it is given by [Grunwaldt et al., 2006]

$$\Delta\bar{R} = \frac{\sum_k S_k \cdot \Delta R_k}{\sum_k S_k}, \tag{4.28}$$

[4] https://ilrs.cddis.eosdis.nasa.gov/missions/satellite_missions/current_missions/index.html

[5] https://ilrs.cddis.eosdis.nasa.gov/missions/satellite_missions/current_missions/swma_reflector.html

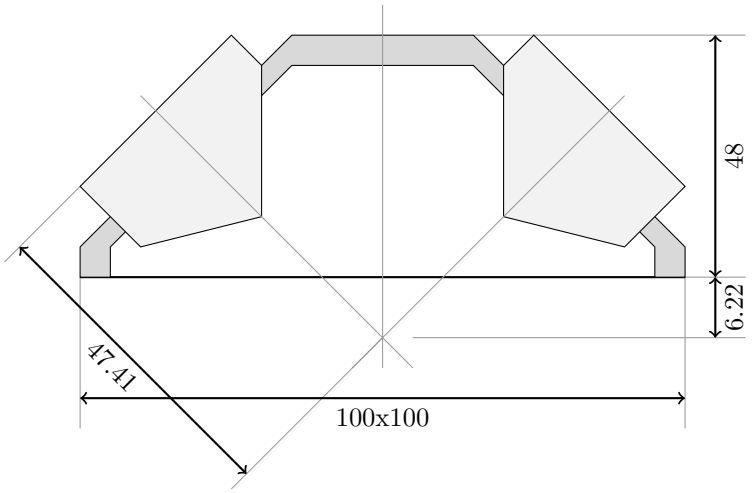

Figure 4.5: Schematic side view of LRR array manufactured at GeoForschungs Zentrum Potsdam with the measurements provided in [Neubert et al., 1998].

Table 4.4: Specification of the LRR geometry, given by [Neubert et al., 1998].

Property	**Value**
Vertex Length	28 mm
Clear aperture of the front face	38 mm
Distance prism front face to reference point	47.41 mm
Index of refraction for 532 nm	1.461

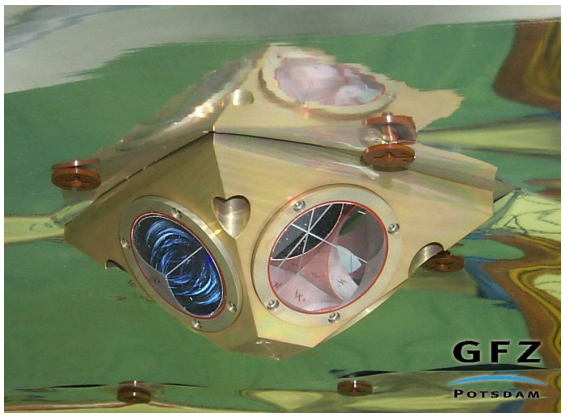

Figure 4.6: Image of the LRR array manufactured at GeoForschungs Zentrum Potsdam, Courtesy of GFZ.

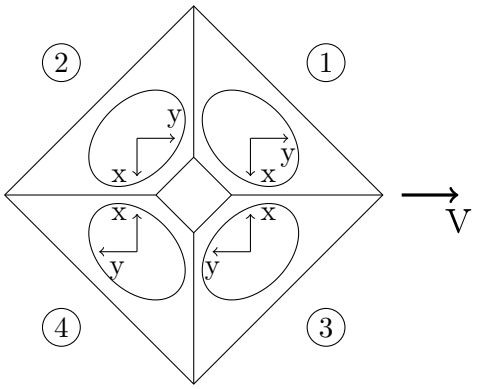

Figure 4.7: Schematic prism axis alignment as seen from ground, with V as the satellite's velocity vector as given in [Grunwaldt et al., 2006].

with the range correction of a single prism k given by

$$\Delta R_k = D\cos(\alpha) - L \cdot \sqrt{n^2 - \sin(\alpha)^2} \tag{4.29}$$

with L as the vertex length, D as the distance of the prism front face to the reference point, n as the index of refraction and α as the angle between the incoming laser and the normal of the prism front face. The relative intensities S_k depend mainly on the location of the station from the prism's prospective and can thus be approximated by

$$S_k = \left(1 - \frac{\alpha_k}{0.85}\right)^2 \tag{4.30}$$

[Neubert et al., 1998][Grunwaldt et al., 2006].

For the determination of the incident angle α_k the vector of the LRR to the station in the SC reference frame $\rho_{S/C}^{Station}$ had been transformed into a separate coordinate system for each prism with the axes aligned as depicted in figure 4.7. α is then given as the angle between the respective prism coordinate system's z-axis (orthogonal to the front face of the prism) and the vector $\rho_{S/C}^{Station}$.

A good estimate can be achieved by neglecting any prisms interference and taking only the most dominant prism. This results in a good approximation with errors in the range below 1 mm [Grunwaldt et al., 2006]. This simplification was applied for the implementation of this error term. The resulting incident dependent errors, depicted in figure 4.8, looks very similar to the reference error pattern given in [Grunwaldt et al., 2006].

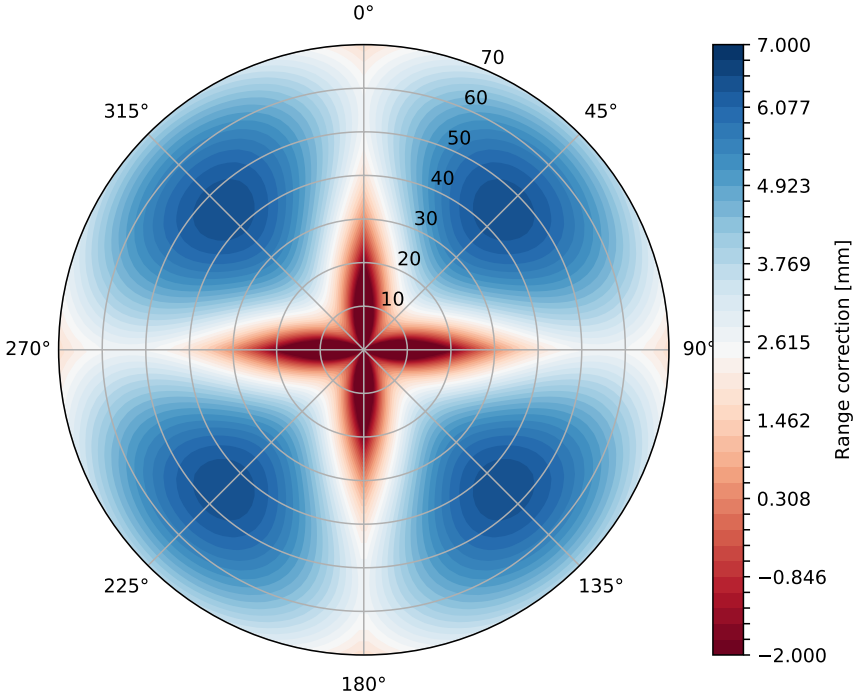

Figure 4.8: Incident dependent LLR bias from implementation. The resulting error pattern matches the reference error pattern given by [Grunwaldt et al., 2006].

Chapter 5

Implementation

The aim of the thesis was to create a software capable of validating given PODs by SLR observations. The basis for this task was an already existing software project which has been extended in order to make it capable of reading SLR observation files and compare them to precomputed distances after applying several correction terms. It is referred to as Gravity Recovery Object Oriented Programming System (GROOPS) and is briefly described in the following section.

The majority of work was invested into testing the implementation with a huge number of observations. Therefore most of the test setup, file handling and data visualization has been highly automated by custom-made scripts as described in section 5.6.

5.1 GROOPS

The GROOPS software is a tool developed and maintained by the Theoretical Geodesy and Satellite Geodesy working group at the Institute of Geodesy (IfG) at Graz Technical University. The software is dedicated to all kinds of geodesy related tasks as well as data handling, conversion and visualization.

It was initially created by Prof. Dr.-Ing Mayer-Gürr during his studies at University of Bonn, Germany. Since 2011 it is developed further and maintained at IfG. The software is implemented in C++ (with small portions in FORTRAN) and features a modular approach where one or more so called "programmes" can be arranged in a script-like manner in order to conduct complex geodetical calculations. Those scripts are written in Extensible Markup Language (XML)-format (cf. section A.2) and serve as command-line input for the actual software. They are from now on referred to as *scenarios*. As in 2018 the software is compromised of 356 individual programmes. For the scope of this thesis two additional programmes, denoted *ReadSlrNormalPoints* and *SlrValidation* have been added.

5.2 GROOPS GUI

In addition to the command-line programme there exists a Graphical User Interface (GUI), which allows the generation of XML input files in a simple building brick manner. A screenshot of the typical appearance of the GUI is depicted in figure 5.1. Besides the

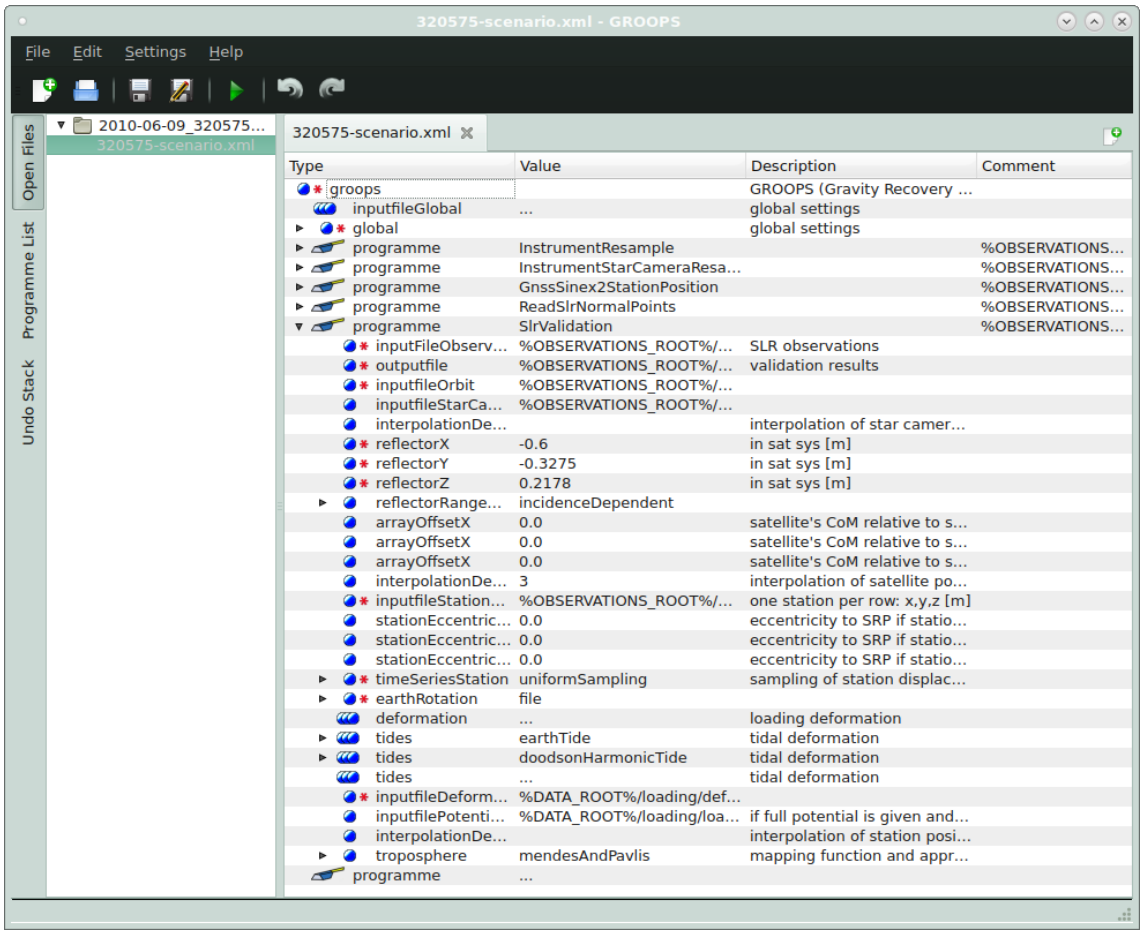

Figure 5.1: Screenshot of the GUI for GROOPS on a Debian system with MATE desktop environment.

programme itself, most programmes additionally require several optional or mandatory parameters.

While being used for debugging of the newly implemented modules and template scenario setup, the GUI has not been used for actual testing, which was conducted by editing the scenario files directly with scripts.

5.3 ReadSlrNormalPoints

The first programme developed is labeled *ReadSlrNormalPoints*. Its task is to read an observation file given in the CRD format (cf. section A.4), detect all lines containing observations and save them in a GROOPS-readable structured matrix into the specified output file. The same procedure is applied to all meteorological records which are saved to a separate file containing only meteorological records and the laser wave length. Table 5.1 describes all the input parameters as presented by the GROOPS GUI.

In addition to reading some of the data is reformatted, e.g. UTC timestamps converted to GPS (which is used internally by GROOPS), and some sanity checks of the raw

Table 5.1: Inputs for the GROOPS programme *ReadSlrNormalPoints*.

Label	Description
inputFile[1]	The raw observations file in CRD format (cf. section A.4)
outputFileMetro[1]	Output file containing metrological- and laser related data
outputFileObservations[1]	Output file containing the observation records

[1] Mandatory input

observation file, e.g. checking for presence of *end-of-session* and *end-of-file* records, is conducted.

5.4 SlrValidation

The core functionality for the validation process is housed in a GROOPS programme labeled *SlrValidation*. It takes the inputs provided by the *ReadSlrNormalPoints* programme (cf. section 5.3) as well as a POD of the satellite for the epochs of the SLR observations, time series of the satellite's star camera orientation, site position in ITRF, setup specific parameters and additionally inputs needed for modeling the station displacements. All input parameters as well as their description are given in table 5.2.

The output is written to an output file in form of matrix with one line per epoch and columns for epoch of observation, predicted range, observed range, residuum and various correction terms.

The general workflow of the programme could be described as follows;

- For each epoch in the satellite's orbit the LRA offset, rotated according to the star camera attitude is added to the satellite's position.
- For the station position the eccentricity to SRP (if present) is added. Time series for the same epochs as the satellite orbit are created with various displacements applied.
- All the SLR observations are read in with their epochs and observed flight times.
- For each SLR observation a predicted range d_p is calculated by taking the one-way distance between the corrected and interpolated station position (with Earth rotation applied) at epoch and the corrected and interpolated reflector position on the satellite at epoch.
- All corrections from the extended observation equation 4.2 are applied to the range calculated from the time of flight, giving the observed distance d_o.
- For each observation the residual d_r is calculated by

$$d_r = d_o - d_p. \tag{5.1}$$

Table 5.2: Inputs for the GROOPS programme *SlrValidation*.

Label	Description
inputfileObservations[1]	Input file containing the formatted observations resulting from *readSlrNormalPoints*
outputFile[1]	Output file for the final results
inputfileOrbit[1]	Input file for the respective satellite orbit
inputfileStartCamera	Input file for the transient start camera attitude
interpolationDegreeStarCamera	Degree of the polynomial interpolating the satellite star camera attitude *(Default: 3)*
reflectorX[1]	LRR offset, x-coordinate, in meters
reflectorY[1]	LRR offset, y-coordinate, in meters
reflectorZ[1]	LRR offset, z-coordinate, in meters
reflectorRangeCorrection[2]	Incident dependent LRR correction, *(Default: <none>)*
arrayOffsetX	Array offset, x-coordinate in meters
arrayOffsetY	Array offset, y-coordinate in meters
arrayOffsetZ	Array offset, z-coordinate in meters
interpolationDegreeSatellite	Degree of the polynomial interpolating the satellite's position *(Default: 3)*
inputfileStationPosition[1]	File containing the stations x,y and z-coordinates in meters
stationEccentricityToSRPNorth	North component of stations eccentricity to SRP in meters
stationEccentricityToSRPEast	East component of stations eccentricity to SRP in meters
stationEccentricityToSRPUp	Zenit component of stations eccentricity to SRP in meters
timeSeriesStation[1]	Sampling of the given station positions *(Default: uniformSampling)*
earthRotation[1]	Earth rotation *(Default: file)*
deformation	Multiple inputs modeling the deformation
tides	Multiple inputs modeling tidal inflicted deformation
inputfileDeformationLoadLoveNumber[1]	Deformation load love numbers
inputfilePotentialLoadLoveNumber	Potential load love numbers
interpolationDegreeStation	Degree of the polynomial interpolating the station position *(Default: 5)*
troposphere[3]	Applied model for the tropospheric delay

[1] Mandatory input

[2] Input can be selected via drop-down list. They are referred to together with their option-dependent input parameters in table 5.3.

[3] Troposphere model can be selected from a drop-down list. Table 5.4 describes the options relevant for *SlrValidation*.

Table 5.3: Options for the *reflectorRangeCorrection* input in the *SlrValidation* programme. The different selections are discussed in section 4.7.

Label	Description
Option: <none>	
Option: constantValue	
constantCorrection[1]	Constant correction offset added to observations in meters
Option: incidentDependent	
vertexLength[1]	Length of the vertex (cf. section 4.7)
distanceToReference[1]	Distance of the front face of the prism to the reference point in meters
indexOfRefraction[1]	Index of refraction

[1] Mandatory input

Table 5.4: Options for the *troposphere* input in the *SlrValidation* programme. The different selections are discussed in section 4.5.

Label	Description
Option: <none>	
Option: mariniAndMurray	
inputFileMetro[1]	The file containing the metro records, resulting from *readSlrNormalPoints*, section 5.3
Option: mendesEtAl	
inputFileMetro[1]	The file containing the metro records, resulting from *readSlrNormalPoints*, section 5.3
mappingFunction[1]	Function mapping the elevation depent amplification of the tropospheric delay (cf. section 4.5.3) *(Default: FCULa)*

[1] Mandatory input

5.5 Troposphere

For modeling the troposphere GROOPS already features a *Troposphere* class. Two derived classes *TroposphereMariniAndMurray* and *TroposphereMendesEtAl* have been added to model the troposphere models presented in section 4.5. Upon initialization all meteorological records and their respective epochs are loaded. The tropospheric delay is returned by a class method, which takes the observation epoch and the elevation to the satellite as parameters. The atmospheric parameters at the site at epoch are approximated by linear interpolation of the meteorological records as recommended in [Ricklefs, 2006].

5.6 Testing

Due to the shear number of observations and scenarios necessary for a thorough testing of the implementation the setup, processing and post-processing was automated to a high degree.

One testing scenario is compromised of 5 GROOPS programmes: 2 resampling programmes for the given satellite orbit and star camera time series, the *ReadSlrNormalPoints* programme, a programme for reading the station position in SINEX format and giving them in Cartesian coordinates and the core of the scenario, the *SlrValidation* programme. A complete flow chart of the interaction of all the programmes with input and intermediate files is presented in figure 5.2.

The setup has been such that there was one such scenario dedicated to excatly one SLR observation file, which in turn contains between one and infinite (usually between two and twenty) single NP observations at different epochs.

Most of the automated setup and later postprocessing has been done using Python scripts. Overall, the testing process contained four different steps:

Observations retrieval: The observation files in CRD data format (cf. section A.4) were provided by EUROLAS Data Center (EDC)[1]. For automated retrieval the Application Programming Interface (API) was used, which can be operated by means of simple POST requests with predefined parameters.

The station positions in ITRF are provided on a daily basis by CDDIS[2] in SINEX format (cf. section A.3).

Scenario setup: This step involved setting up the folder structure with additional input files necessary for the validation. A XML execution file which serves as input for the GROOPS programme was created. Each scenario has a dedicated folder which holds up to 10 files as specified in table 5.5.

Execution of scenarios: The previously created XML file is executed by the GROOPS software and an execution log is saved to the respective folder.

Postprocessing: The final step deals with selecting, filtering and visualization of the results as well as calculating representative values such as RMS.

[1] `https://edc.dgfi.tum.de/en/`. Another source for SLR observations is the Crustal Dynamics Data Information System (CDDIS) which provides the data through a public accessible FTP server at `ftp://cddis.gsfc.nasa.gov/`

[2] `ftp://cddis.gsfc.nasa.gov/pub/slr/products/pos+eop/`

Table 5.5: Folder contents of a typical scenario folder.

Filename	Description
<observation_id>-scenario.xml	The input XML for the GROOPS programme
<observation_id>-station_id.txt	Plain text file containing the station id
<observation_id>-station_position.xml	Station position in TRF for certain epoch
<observation_id>-satellite_position.xml	Resampled satellite positions for necessary epochs
<observation_id>-star_camera.txt	Resampled star camera alignment for necessary epochs
<observation_id>-metro.xml	Metrological parameters of the observation in XML
<observation_id>-observations.txt	Observation records
<observation_id>-crd.txt	Raw observations file in CRD format
<observation_id>-execution.log	Execution log produced by GROOPS
<observation_id>-results.txt	Formatted results

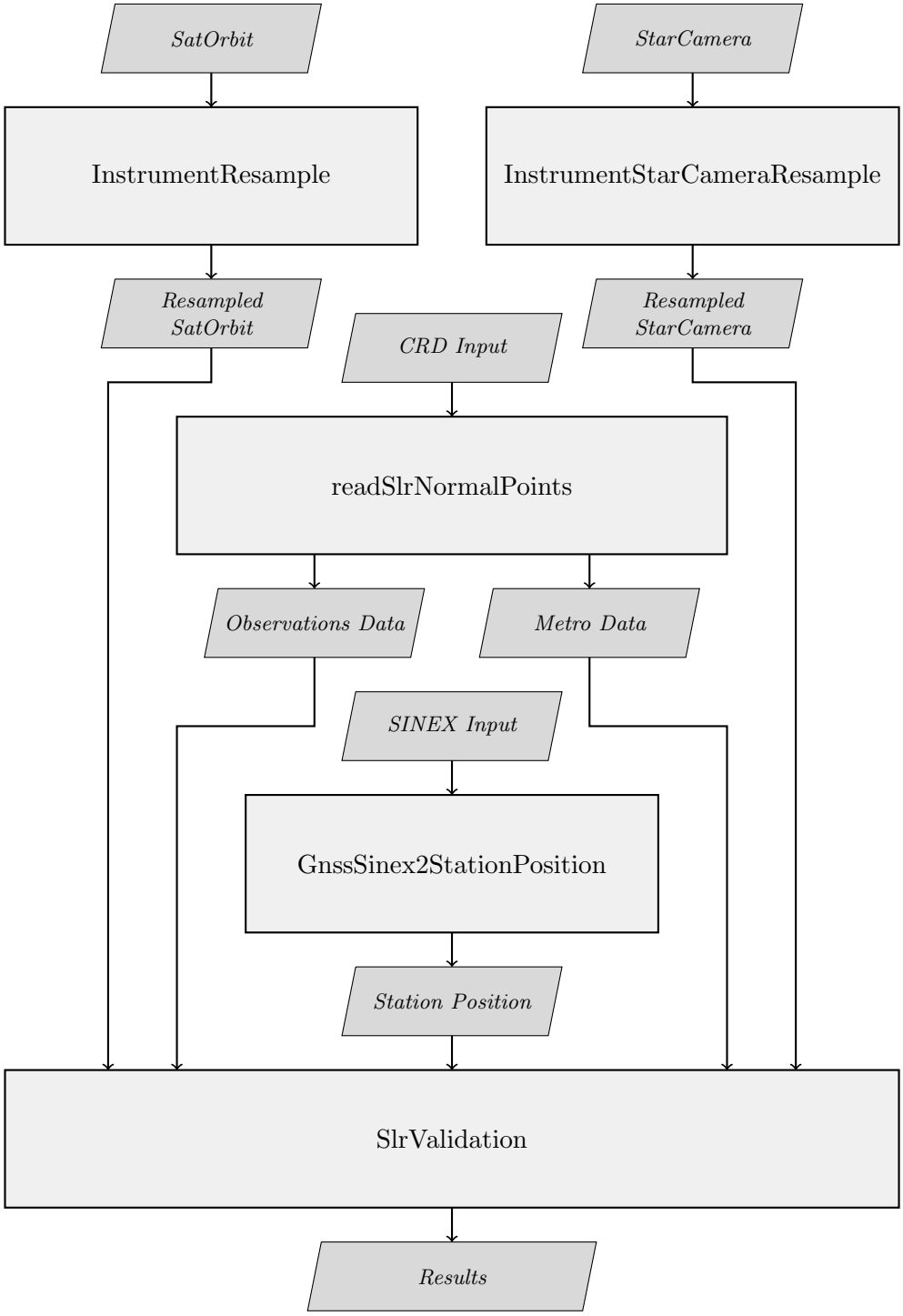

Figure 5.2: Program Flow Chart of a single scenario with all applied programmes and intermediate files.

Chapter 6

Results

In order to test the implementation the measured distances of SLR observations have been compared to an expected distance given by station position and satellite POD as described in section 5.6. The quality of an observation is given by the magnitude of the residual which is given by equation 5.1.

The focus has been on PODs of the 2 satellites of the GRACE- (cf. section 3.2) and the 3 satellites of the Swarm (cf. section 3.1) missions. The first section of this chapter documents how the obtained results were preprocessed and filtered. The second section investigate the quality of different POD types, including kinematic and dynamic PODs and the third section compares the POD solution from different facilities, which are IfG at Graz University of Technology, TU Delft (TUD) and the Astronomical Institute at the University of Bern (AIUB). The last section compares different tropospheric delay models and mapping functions.

6.1 Preprocessing of results

In order to achieve scientifically representative results, the raw results were processed further. As a first step gross outliers, which are a result of setup errors or faulty measurements, were removed. This has been done by removing observations whose absolute residuals exceeded a generously defined threshold.

Additionally, observations with an elevation angle below 20 degrees were omitted. Those measurements have to deal with a comparably long way through the Earth's atmosphere and the applied tropospheric delay models perform poorly at low elevation angles. The left side of figure 6.1 displays the distribution of an arbitrary selection of measurements for different elevation angles. The worsening of the results for lower elevation angles is thereby clearly visible. Another reason to set the limit to 20 degrees is that some observation sites, e.g. Wetzell or Potsdam, do not publish observations which are below this angle. This is also clearly visible in figure 6.1 as a leap in density of measurements at 20 degrees.

The elevation dependent quality of observation was also investigated from a satellite's perspective as depicted on the right side of figure 6.1. Similarly to the elevation angles from a station's perspective a deterioration at small angles is observable. At the same time almost no measurements have an elevation angle below 20 degrees. Hence, no elevation

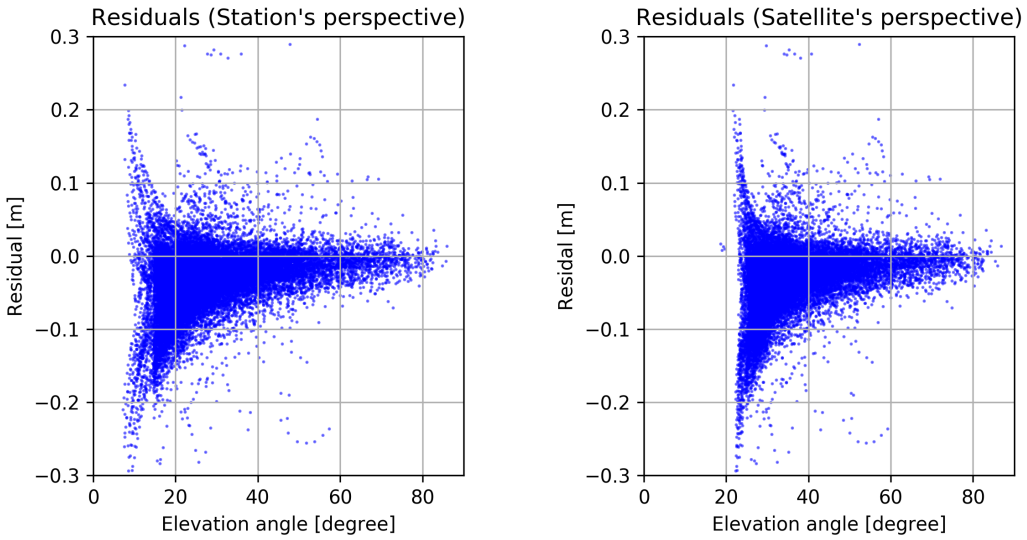

Figure 6.1: Residuals distribution for elevation angles. Observations of the GraceA mission between 2010 and 2011 from various stations.

mask was applied there.

After theses steps a dynamic filter was applied to the remaining observations, removing observations whose Root-Mean Square (RMS) exceeded the overall RMS by more than five times. After each iteration the overall RMS was recomputed. This was repeated until the overall RMS did not change significantly from one iteration to the next.

The last step involved removing the arithmetic mean $\bar{x}$ from the remaining observations. It is given by

$$\bar{x} = \frac{1}{N} \sum_{i=0}^{N} x_i \tag{6.1}$$

with N as the number of individual observations.

6.2 Comparison of POD types

In total, three different POD types (cf. section 2.4), including a *kinematic fixed*, a *kinematic float* and a *reduced dynamic* type have been compared to each other.

The subject of investigation have been the PODs of the GRACE mission in the time between January 2010 and December 2011, which have been established by Dr. Zehentner within the scope of his doctoral thesis [Zehentner, 2017] at Graz University of Technology. The PODs were provided in the internal GROOPS data format on a monthly basis. For the specified timespan a total of 5 736 valid observation sessions, performed by 8 different sites have been selected, containing an overall of 56 192 observations, as specified in table 6.1.

The monthly RMS for the GraceA and GraceB satellites after preprocessing is depicted in figure 6.2 and their overall RMS values are given in table 6.2.

All POD types yield RMS values in the range of 3 to 4 cm. The *reduced dynamic* POD

Table 6.1: Observation sources for GraceA and GraceB between January 2010 and December 2011.

Satellite	Code	Station	Sessions	Observations
GraceA	YARL	Yarragadee, Australia	2052	15218
	GRZL	Graz, Austria	322	6201
	MONL	Monument Peak, California	255	3184
	MATM	Matera, Italy (MLRO)	126	2061
	HARL	Hartebeesthoek, South Africa	80	1250
	HA4T	Haleakala, Hawaii	26	331
	BEIL	Beijing, China	23	302
	MDOL	McDonald Observatory, Texas	5	29
Total			**2889**	**28576**
GraceB	YARL	Yarragadee, Australia	1993	14084
	GRZL	Graz, Austria	309	5519
	MONL	Monument Peak, California	243	2788
	HARL	Hartebeesthoek, South Africa	105	2289
	MATM	Matera, Italy (MLRO)	133	2036
	HA4T	Haleakala, Hawaii	39	593
	BEIL	Beijing, China	22	289
	MDOL	McDonald Observatory, Texas	3	18
Total			**2847**	**27616**

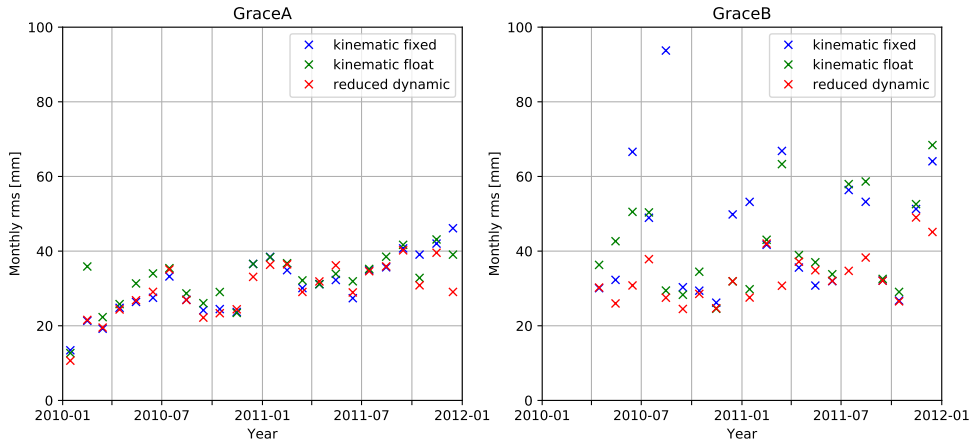

Figure 6.2: Comparison of RMS of different orbital solutions for the period January 2010 to December 2011 on monthly basis.

Table 6.2: Comparison of yearly RMS with arithmetic mean removed for GraceA and GraceB and different POD types.

Satellite	Year	kinematic fixed RMS (Mean)[mm]	kinematic float RMS (Mean)[mm]	reduced dynamic RMS (Mean)[mm]
GraceA	2010	24.7974 (-22.9415)	27.6664 (-22.2254)	24.9635 (-26.7177)
	2011	36.0599 (-26.1031)	36.2146 (-26.8625)	34.0899 (-24.1843)
GraceB	2010	45.2598 (-25.8218)	36.4911 (-25.6251)	28.9511 (-28.0214)
	2011	45.3560 (-26.1045)	45.4419 (-26.9511)	35.8053 (-22.9588)
Total		**37.8682 (-25.2427)**	**36.4535 (-25.4160)**	**30.9525 (-25.4706)**

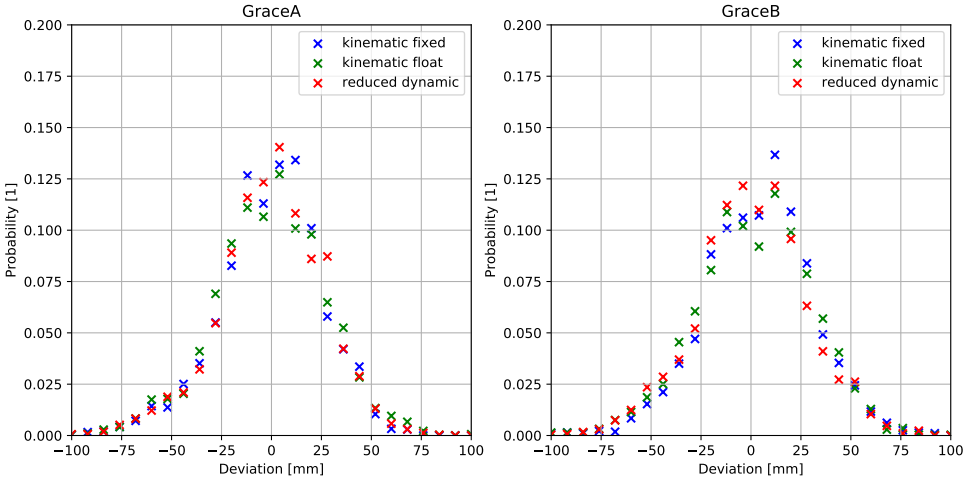

Figure 6.3: Gaussian distribution of GraceA and GraceB observations for the period January 2010 to December 2011 and different POD types.

type performed best, followed by the *kinematic float* and *kinematic fixed* POD type. It could not be established why all of the PODs performed worse for the year 2011. Also, the results feature a rather high arithmetic mean values in the range between -2 and -3 cm in every observation group for every observation period.

A probability distribution of the residuals is given in figure 6.3. It resembles a Gaussian distribution but with some unobtrusive wave characteristics. For both satellites and all POD types there are clearly more residuals on the negative part of the x-axis and thus observations underestimating the observed distance. All POD types display a very similar distribution.

Sky plots from a station's-, as well as from a satellite's perspective have been established as depicted in figure 6.4 and 6.5. Apart from generally worse estimates at low elevation angles there is no systematic bias visible. Larger deviations appear seemingly random for any azimuth and elevation angle.

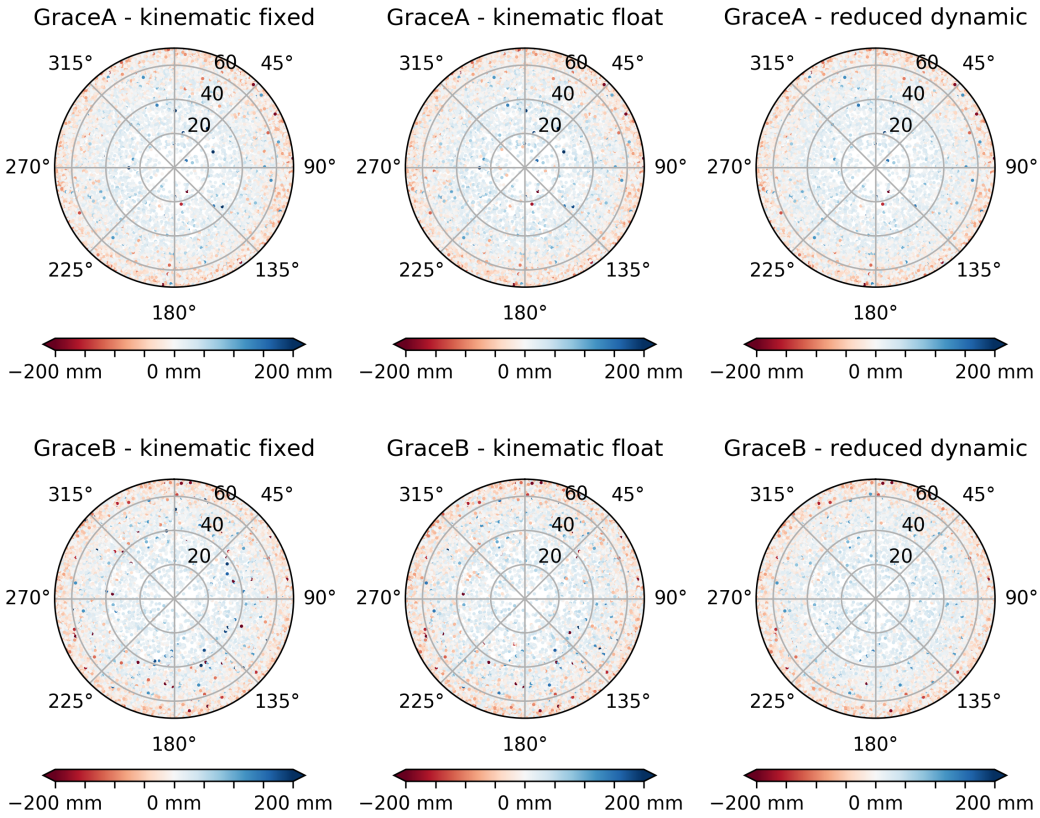

Figure 6.4: Skyplots of GraceA and GraceB observations from January 2010 to December 2011. The color code indicates the magnitude of the residuals.

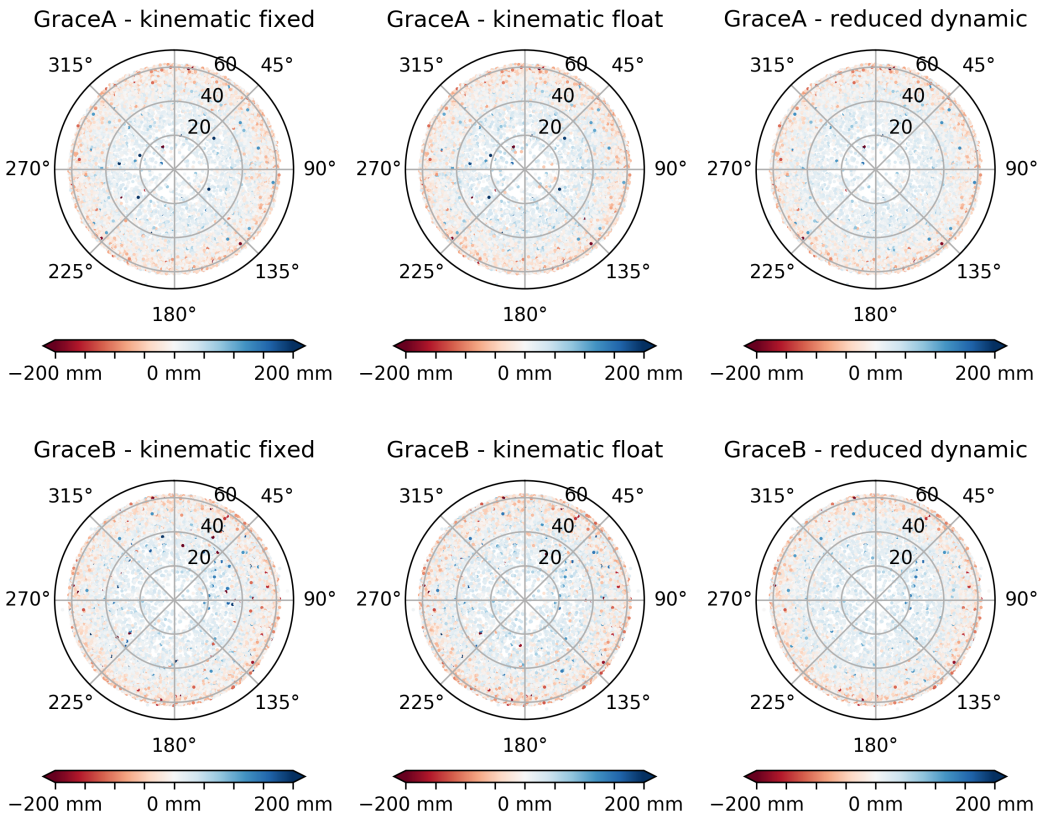

Figure 6.5: Skyplots of GraceA and GraceB observations from January 2010 to December 2011 from the satellite's perspective. The color code indicates the magnitude of the residuals.

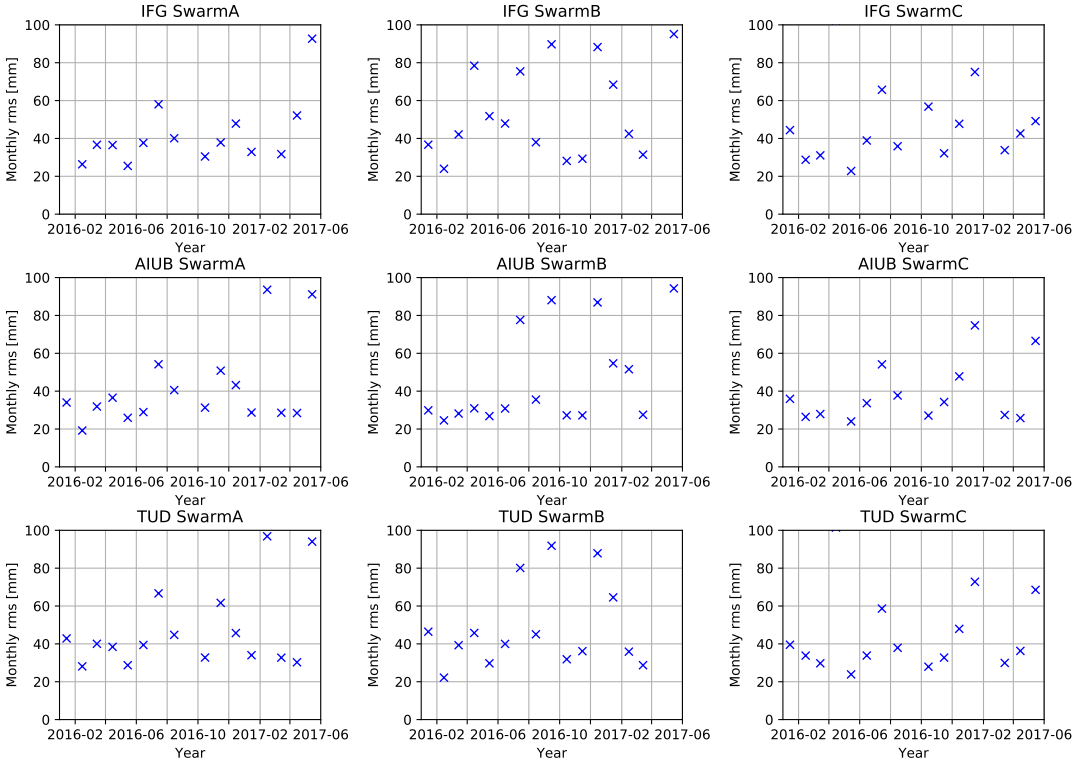

Figure 6.6: Comparison of monthly RMS of SwarmA, SwarmB and SwarmC for kinematic PODs by IfG, AIUB and TUD for the period between January 2016 and August 2017.

6.3 Comparison of POD solutions

The POD solutions by IfG have also been compared to solutions calculated by other facilities. In particular, the orbits of the three satellites of the Swarm mission (cf. section 3.1) in the period between January 2016 and August 2017 have been compared. Apart from the solution by IfG, the solutions by AIUB and TUD have been considered. All of them have been of kinematic float POD type.

In total 47 888 observations from 2 335 individual observation sessions conducted by 10 different SLR sites, as depicted in table 6.3, have been selected. Validation of the preprocessed data yielded the monthly RMS values as depicted in figure 6.6, with the overall RMSs and arithmetic means listed in table 6.4.

The RMS values are in the range from 5 to 6 cm with arithmetic means of -2 to -3 cm. Apparently the solution by AIUB performed slightly better than the solutions by IfG and TUD. Compared to the GRACE observations the results for the Swarm satellites performed generally worse, what is in accordance with the results by [Zehentner, 2017].

Table 6.3: Observation sources for the Swarm mission satellites between January 2016 and August 2017.

Satellite	Code	Station	Sessions	Observations
SwarmA	GODL	Greenbelt, Maryland	230	4075
	MONL	Monument Peak, California	271	2409
	HARL	Hartebeesthoek, South Africa	93	1382
	GRZL	Graz, Austria	67	1030
	SHA2	Shanghai, China	49	654
	SVEL	Svetloe, Russia	17	148
	IRKL	Irkutsk, Russia	7	47
	MATM	Matera, Italy (MLRO)	4	42
	ARKL	Arkhyz, Russia	1	22
	GLSL	Golosiiv, Ukraine	1	10
Total			**740**	**9819**
SwarmB	GODL	Greenbelt, Maryland	276	10070
	MONL	Monument Peak, California	214	7484
	GRZL	Graz, Austria	114	4595
	HARL	Hartebeesthoek, South Africa	143	4073
	SHA2	Shanghai, China	69	1282
	SVEL	Svetloe, Russia	49	530
	MATM	Matera, Italy (MLRO)	11	131
	IRKL	Irkutsk, Russia	9	58
	ARKL	Arkhyz, Russia	2	25
	GLSL	Golosiiv, Ukraine	1	12
Total			**888**	**28660**
SwarmC	GODL	Greenbelt, Maryland	205	3470
	MONL	Monument Peak, California	259	2231
	HARL	Hartebeesthoek, South Africa	92	1667
	GRZL	Graz, Austria	75	1164
	SHA2	Shanghai, China	52	656
	SVEL	Svetloe, Russia	17	163
	GLSL	Golosiiv, Ukraine	4	35
	IRKL	Irkutsk, Russia	2	17
	MATM	Matera, Italy (MLRO)	1	6
Total			**707**	**9409**

Table 6.4: RMS values with arithmetic means removed of SwarmA, SwarmB and SwarmC PODs by IfG, AIUB and TUD for the period between January 2016 and August 2017.

Facility	Orbit	Mean RMS [mm]	Arithmetic Mean [mm]
IfG	SwarmA	57.0022	-27.5283
	SwarmB	57.6660	-31.2093
	SwarmC	55.4230	-35.9586
	Total	**56.6971**	**-31.5654**
AIUB	SwarmA	45.9022	-22.4661
	SwarmB	50.3159	-25.5815
	SwarmC	51.6759	-28.3114
	Total	**49.2980**	**-24.5403**
TUD	SwarmA	51.6178	-29.6722
	SwarmB	55.2536	-31.7921
	SwarmC	53.2805	-34.5069
	Total	**53.3840**	**-31.9904**

6.4 Comparison of tropospheric models

For the baseline version of the SLR validation programme two different models for the estimation of the tropospheric delay have been implemented. Those are the model by Marini and Murray from 1973 (cf. section 4.5.1) and the model by Mendes et al. from 2002 (cf. section 4.5.2). In the latter the mapping function is completely independent from the delay in zenith direction. Thus, different models for the mapping function can be used independently to estimate the overall tropospheric delay of a specific scenario. For the scope of this thesis the mapping functions FCULa and FCULb by Mendes et al. [Mendes and Pavlis, 2004] (cf.section 4.5.3) have been implemented.

This yields three possible settings for the tropospheric delay modeling, which have been compared to each other for the observations of the GraceA satellite in the period between January 2010 and December 2011. The number of used observations and their distribution to observation sites is as depicted in table 6.7. The resulting monthly RMS values are depicted in figure 6.7 with their overall values in table 6.6.

Judging by these values, it can be clearly seen that the more recent model by Mendes et al. is far superior to the model by Marini and Murray which has a very high arithmetic mean of more than -10 cm. The difference between the mapping functions FCULa and FCULb is visually hardly distinguishable. Thus, the difference of the monthly RMS has been calculated (cf. figure 6.8). Those are in the lower sub-mm-range.

Figure 6.9 features the distribution of residuals for the tested tropospheric models over the elevation angle. In the model by Mendes et al. a rising fluctuation with decreasing elevation angle is clearly visible. Also, a slightly askew distribution, with more residuals being in the negative area can be observed.

The model by Marini and Murray on the other hand clearly contains some trend.

Figure 6.10 shows the tropospheric range corrections applied for various models and all observations. There are three aspects derivable from this plot. Firstly, the range corrections done with the model by Mendes et al. and different mapping functions do

Table 6.5: Observation sources for GraceA between January 2010 and December 2011.

Code	Station	Sessions	Observations
YARL	Yarragadee, Australia	2052	15218
GRZL	Graz, Austria	322	6201
MONL	Monument Peak, California	255	3184
MATM	Matera, Italy (MLRO)	126	2061
HARL	Hartebeesthoek, South Africa	80	1250
HA4T	Haleakala, Hawaii	26	331
BEIL	Beijing, China	23	302
MDOL	McDonald Observatory, Texas	5	29
Total		**2889**	**28576**

Table 6.6: RMS values with arithmetic means removed for GraceA and tropospheric models by Marini and Murray and Mendes et al.

Tropospheric Model	MF	Mean RMS [mm]	Arithmetic Mean [mm]
Marini and Murray	-	39.6071	-107.0668
Mendes et al.	FCULa	29.4215	-25.4540
Mendes et al.	FCULb	29.5225	-25.2537

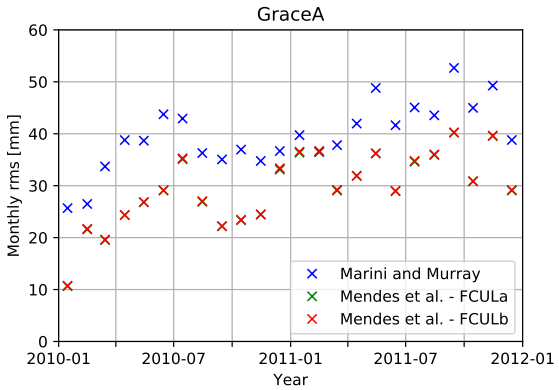

Figure 6.7: Monthly RMS values for GraceA observations in the period between January 2010 and December 2011 for different tropospheric models.

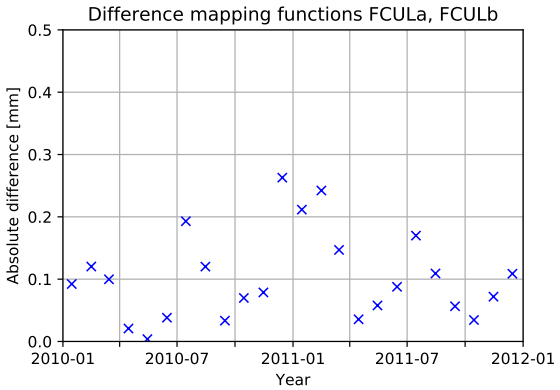

Figure 6.8: Absolute difference between mapping functions FCULa and FCULb for the monthly RMS values depicted in figure 6.7.

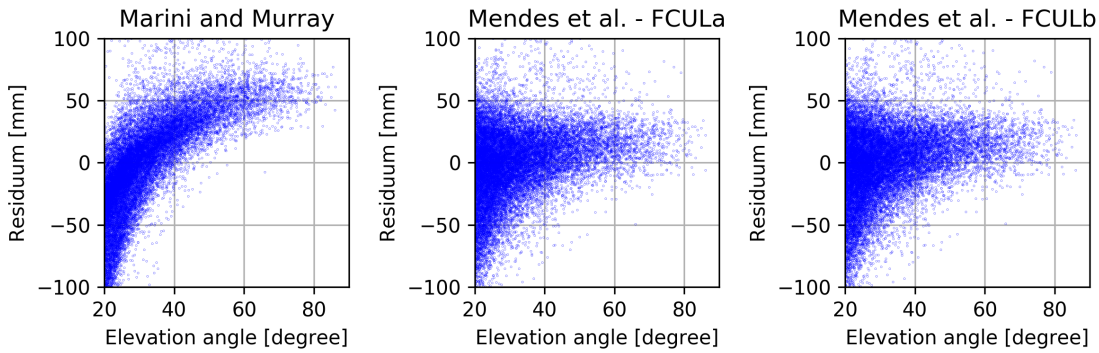

Figure 6.9: Residuals of different tropospheric models for elevations.

not visibly differ from one another (as pointed out above). Secondly, the different models seem to yield similar results but with a constant offset. This is in accordance with table 6.6 where the model by Marini and Murray has a high arithmetic mean with an absolute of more than 10 cm.

Lastly, it can be seen that the corrections appear in four separate bands with none of them populating the areas in between. It has been established that this is due to the dependence of the correction models on station location with an limited variety of latitude, height combinations of used stations from table 6.5.

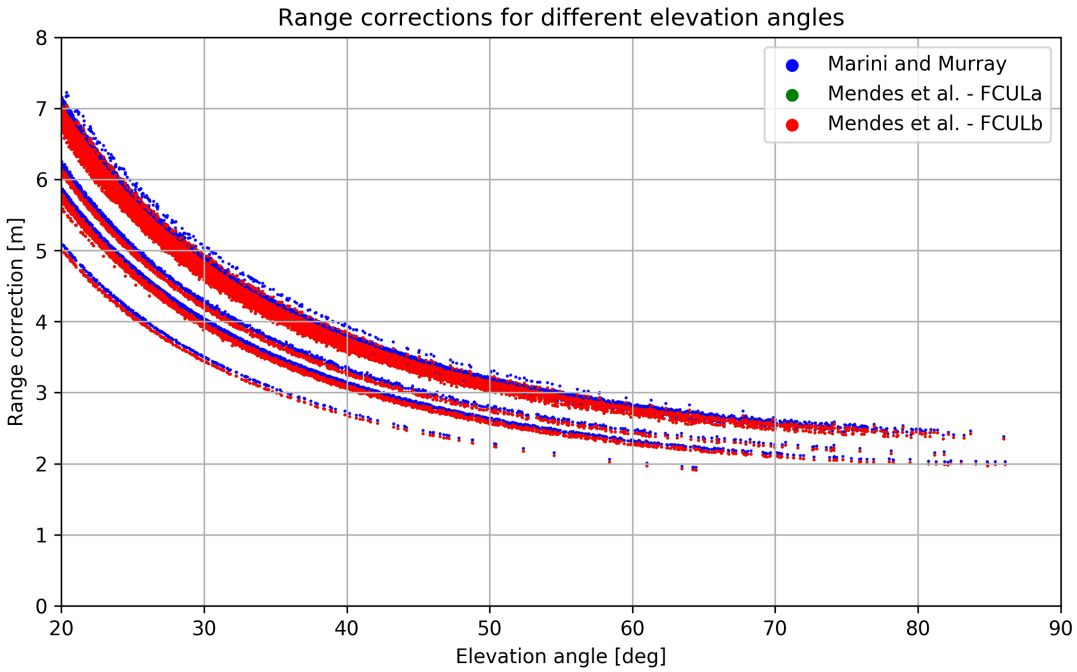

Figure 6.10: Range correction values of different tropospheric models for elevations.

Chapter 7

Conclusion and Outlook

Within the work for this thesis the GROOPS software was extended by the two programmes *ReadSlrNormalPoints* and *SlrValidation* and additional troposphere classes.

Testing by comparison to expected ranges, estimated by means of PODs showed that in general, all accuracies are in the range of a few centimeters. The comparison of POD types in section 6.2 resulted in an overall RMS of 37.87 mm for kinematic fixed-, 36.45 mm for the kinematic float- and 30.95 mm for the reduced dynamic type. Thus, the reduced dynamic POD performed clearly superior to the kinematic types. All observations of Grace satellites featured an unexpected high arithmetic mean in the range of -2.5 cm to -3 cm. This might indicate that some systematic error is still present. The source and characteristic of this error could not be established.

The comparison of kinematic POD solutions by different facilities showed accuracies of about 5 cm for all facilities for Swarm satellite orbits. The solution by AIUB performed best with an overall RMS of 49.30 mm, followed by TUD with 53.38 mm and IfG with 56.79 mm. Those results are approximately in the range determined by [Zehentner, 2017], but like the GRACE orbits the Swarm orbits validations showed an unexpected high arithmetic mean.

In terms of refraction correction, two different models have been evaluated. According to the results in section 6.4 the model by Marini and Murray is inferior to the more recent model by Mendes et al. Thus, the latter should be used for precise validations. The results obtained with the different mapping functions FCULa and FCULb, which have been used in combination with the model by Mendes et al., are hardly distinguishable. The claim in [Mendes et al., 2002] that FCULa generally performs better than FCULb could thus not be verified. Also, the largest differences in the mapping function are in the Asian and southwest Pacific regions which have a low density of observation stations.

Further advancements in accuracy could be made by implementing more precise refraction correction models, once such models are developed, or by investigating other mapping functions. Although the applied FCULa mapping function is the one recommended by IERS conventions there exists a variety of others which could perform better for specific site locations or elevation angles.

Appendix A

Data Formats

A.1 ILRS Site and System Information Form

The ILRS Site and System Information form is used for the thorough description of the SLR system at a certain site.

The logs are publicly available at the FTP server at `ftp://cddis.gsfc.nasa.gov/slr/slrlog/` and feature a naming convention including the 4-letter site code as well as the submission date like

`SSSS_YYYYMMDD.log`.

For example, the current log (state October 3, 2018) for station Graz Lustbühel is labeled `grzl_20180626.log`.

A new log is issued whenever one or more of the parameters change, thus keeping a history of system parameters. The file is in plain ASCII format and is splitted into 18 sections refered to in table A.1. Each section includes one or more parameters, which are one per line with label and value separated by a colon. Some fields may also take up multiple lines in order to do not exceede the maximum line length of 80 characters.

A thorough and updated description of the format is maintained by the International Laser Ranging Service[1].

A.2 Extensible Markup Language

The Extensible Markup Language is a software and hardware independent format for exchanging and storing structured data. As a markup language it is thereby both; human- and machine readable. The format makes use of user-defined tags, which usually consist of an opening and closing tag enclosing the respective data. The tags can be nested in order to represent complex data structures.

A.3 SINEX data format

The *Solution (Software/ technique) INdependent EXchange Format* (SINEX) was developed by the SINEX Working Group of the *International GNSS Service* (IGS) in the mid

[1] `https://ilrs.cddis.eosdis.nasa.gov/network/site_procedures/site_log_procedure.html`

Table A.1: Sections of the ILRS Site and System Information Form.

Section	Title
0	Form
1	Identification of the Ranging System Reference Point (SRP)
2	Site Location Information
3	General System Information
4	Telescope Information
5	Laser System Information
6	Receiver System
7	Tracking Capabilities
8	Calibration
9	Time and Frequency Standards
10	Preprocessing Information
11	Aircraft Detection
12	Meteorological Instrumentation
13	Local Ties, Eccentricities, and Collocation Information
14	Local Events Possibly Affecting Computed Position
15	On-Site, Point of Contact Agency Information
16	Responsible Agency (if different from 15.)
17	More Information

1995ies. Due to its modular and general design it was later also used for SLR and VLBI observations.

SINEX files are of ASCII format with lines of a maximum of 80 characters. Generally, all the data is organised in predefined blocks with no specific order. The most important blocks are the SOLUTION blocks with some of them being mandatory. Each block consists thereby of a starting line, which consists of the block label and a "+" as prefix, and ends with a closing line which features also the block label and a preceeding "-". All the data inside a block starts with a leading space [IERS, 2006].

Comments can be inserted at any place by prefixing the line with a "%".

A.4 CRD data format

The Consolidated Laser Ranging Data Format (CRD) was developed in order to provide a flexible and extensible for the International Laser Ranging Service (ILRS) data. At the time of this thesis, the format was at version 1.01, which was released by the ILRS Data Formats and Procedures Working Group on 27th October 2009. The format is based on the Consolidated Prediction Format (CPF). The format features a building block fashion, which allows including or ommiting certain record as needed by station or target. Three separate sections:

- Header section
- Configuration section
- Data section

The entries are separated by spaces. Numerical entries set to "-1" are indicating "no inforation", caracter fields "na" for "Not_Available".

A.4.1 Header Records

The Header Records consists of

Format header: The format header starts with "H1" or "h1" and contains the information related to the file.

Station header: The station header, starting with "H2" or "h2", contains information relating to the site.

Session header: The session header, starting with "H4" or "h4". Besides start and end date and time of the observation it also defines the type of the following observation records and an indication on their quality, ranging from "good quality" to "poor or unknown" quality. For this project the only type which was considered was "2 way ranging".

End of session footer: Identified by "H8" and "h8" this record indicates the end of a data session.

End of file footer: Similar to the End of Session Footer this record, starting with "H9" or "h9", is at the end of the file. The absence of this header is an indication that the file is corrupted or truncated.

Furthermore, the header records could feature a target header record, which was of no relevance for the scope of this thesis.

A.4.2 Configuration Records

The Configuration section provides static data on the setup on the observation station. The *System Configuration Record* is the only mandatory record of this section containing information on the wave length of the applied laser which is crucial for the determination of atmospheric delay. Besides, the system configuration there are also *Laser Configuration*, *Detector Configuration* and *Transponder (Clock) Configuration* recods.

A.4.3 Data Records

Holding highly transient information, the data recods always come with a timestamp. Those are given as seconds of day and thus have a float value between 0.0 and 86400.0. Together with the the start and stop times from the Session Header the exact timestamp can be unambigously determined. Furthermore, recods of the same type must be in chronological order.

Meterological data has to be interpolated according to the format specification a 2-point linear interpolation should be sufficient since additional records are only added if one of the values has changed drastically, which is usually not the case of the time of the observation.

For this project the Normal Point Range Records (cf. Normal Point Data 2.5) have been of interest. Those contain an average of multiple measurements concentrated into a single point. The record starts with "11" and contains the entries

- *seconds of day* in GPS time (with an accuracy < 100 ns),
- *time of flight* in seconds,
- *system configuration id*,
- *epoch event* indicating the measurement type. Besides *ground transmit time (at SRP)* (the type used for this project) there exist also the types ground receive time (at SRP), spacecraft bounce time (2 way) and others,
- *normal point window length* in seconds,
- *number of measurements* compressed into the NP,
- and other statistical parameters providing further information on the distribution of measurements of the normal point.

Another important record type is the *Meteorological Record*, prefixed with "20". In contains the meteorological data necessary for the application of the tropospheric correction models. There must be at least one record of this type in each session and every time any of the values changes "significantly", another record has to be added. There necessary entries of this record type include:

- *seconds of day* in GPS time
- *surface pressure* in mbar,
- *surface temperature* in degrees Kelvin and the
- *relative humidity at surface* in percent.

Furthermore the data section might contain the record types:

- Range Record (Full rate, Sampled Engineering/Quicklook),
- Range Supplement Record,
- Meteorological Supplement Record,
- Pointing Angles Record,
- Calibration Record,
- Session (Pass) Statistics Record,
- Compability Record,
- User Defined Record and
- Comment Record.

Appendix B

Acronyms

API	Application Programming Interface
BCRS	Barycentric Celestial Reference System
CCR	Corner Cube Retroreflector
CDDIS	Crustal Dynamics Data Information System
CoM	Center of Mass
CRD	Consolidated Laser Ranging Data
CRF	Celestial Reference Frame
CRS	Celestial Reference System
DORIS	Doppler Orbitography and Radiopositioning Integrated by Satellite
EDC	EUROLAS Data Center
EGM96	Earth Gravitational Model 1996
EOP	Earth Observation Parameters
ESTEC	European Space Research and Technology Centre
GAST	Greenwich Apparent Sidereal Time
GCRS	Geocentric Celestial Reference System
GEOS	Geodetic Earth Orbiting Satellite
GMT	Greenwich Mean Time
GNSS	Global Navigation Satellite Systems
GPS	Global Positioning System
GLONASS	Global Navigation Satellite System
GRACE	Gravity Recovery and Climate Experiment
GROOPS	Gravity Recovery Object Oriented Programming System
GUI	Graphical User Interface
IERS	International Earth Rotation and Reference Systems Service
IGS	International GNSS Service
ILRS	International Laser Ranging Service
IWF	Institut für Weltraumforschung
LRR	Laser Retro Reflector
LLR	Lunar Laser Ranging
LRA	Laser Reflector Array
MF	Mapping Function
NEU	North-East-Up

POD	Precise Orbit Determination
RMS	Root Mean Square
SIC	Satellite Identification Code
SINEX	Solution INdependent EXchange Format
SLR	Satellite Laser Ranging
SRP	System Reference Point
TAI	Temps Atonomique International
TCB	Barycentric Coordinated Time
TCG	Geocentric Coordinate Time
TRS	Terrestrial Reference System
UT1	Universal Time 1
UTC	Universal Time Coordinated
VE	Vernal Equinox
VLBI	Very Long Baseline Interferometry
XML	Extensible Markup Language
ZD	Zenith Delay

Bibliography

[Faust, 2013] Faust, M. (2013). *Swarm Instrument Positions in Spacecraft Coordinates.*

[Grunwaldt et al., 2006] Grunwaldt, L., Flechtner, F., and Rothacher, M. (2006). *GRACE Laser Retro Reflector User Manual.*

[Hofmann-Wellenhof et al., 2003] Hofmann-Wellenhof, B., Legat, K., and Wieser, M. (2003). *Navigation: principles of positioning and guidance.* Springer Verlag Wien.

[House, 1995] House, M. R. (1995). Orbital forcing timescales: an introduction. *Geological Society, London, Special Publications*, 85(1):1–18.

[IERS, 2006] IERS (2006). *SINEX - Solution (Software/technique) INdependent EXchange Format Version 2.10 (September 15, 2006).*

[Jekeli, 2012] Jekeli, C. (2012). *Inertial navigation systems with geodetic applications.* Walter de Gruyter.

[Laurichesse et al., 2009] Laurichesse, D., Mercier, F., BERTHIAS, J.-P., Broca, P., and Cerri, L. (2009). Integer ambiguity resolution on undifferenced gps phase measurements and its application to ppp and satellite precise orbit determination. *Navigation*, 56(2):135–149.

[Mansfeld, 2013] Mansfeld, W. (2013). *Satellitenortung und Navigation: Grundlagen und Anwendung globaler Satellitennavigationssysteme.* Springer-Verlag.

[Marini and Murray Jr, 1973] Marini, J. W. and Murray Jr, C. (1973). *Correction of laser range tracking data for atmospheric refraction at elevations above 10 degrees.*

[Mathews et al., 1995] Mathews, P., Buffett, B., and Shapiro, I. (1995). Love numbers for a rotating spheroidal earth new definitions and numerical values. *Geophysical Research Letters*, 22(5):579–582.

[Melchior, 1974] Melchior, P. (1974). Earth tides. *Geophysical surveys*, 1(3):275–303.

[Mendes and Pavlis, 2004] Mendes, V. and Pavlis, E. (2004). High-accuracy zenith delay prediction at optical wavelengths. *Geophysical Research Letters*, 31(14).

[Mendes et al., 2002] Mendes, V., Prates, G., Pavlis, E., Pavlis, D., and Langley, R. (2002). Improved mapping functions for atmospheric refraction correction in slr. *Geophysical Research Letters*, 29(10):53–1.

[Montenbruck and Gill, 2000] Montenbruck, O. and Gill, E. (2000). *Satellite Orbits: Models, Methods, and Applications*. Springer Science & Business Media.

[Montenbruck and Gill, 2012] Montenbruck, O. and Gill, E. (2012). *Satellite orbits: models, methods and applications*. Springer Science & Business Media.

[Montenbruck et al., 2005] Montenbruck, O., Van Helleputte, T., Kroes, R., and Gill, E. (2005). Reduced dynamic orbit determination using gps code and carrier measurements. *Aerospace Science and Technology*, 9(3):261–271.

[Neubert et al., 1998] Neubert, R., Grunwaldt, L., and Neubert, J. (1998). The retroreflector for the champ satellite: Final design and realization. In *Proceedings of the 11th international workshop on laser ranging*, pages 260–270.

[Pavlis et al., 1999] Pavlis, D., Moore, D., Luo, S., McCarthy, J., and Luthcke, S. (1999). Geodyn operations manual, 5 volumes. *Raytheon ITSS, Greenbelt*.

[Petit and Luzum, 2010] Petit, G. and Luzum, B. (2010). Iers conventions (2010). Technical report, BUREAU INTERNATIONAL DES POIDS ET MESURES SEVRES (FRANCE).

[Plank et al., 2013] Plank, G., Floberghagen, R., Menard, Y., and Haagmans, R. (2013). Swarm: Esa's magnetic field mission. In *AGU Fall Meeting Abstracts*.

[Ray and Ponte, 2003] Ray, R. and Ponte, R. (2003). *Barometric tides from ECMWF operational analyses*.

[Ricklefs, 2006] Ricklefs, R. L. (2006). Consolidated laser ranging prediction format. *ILRS Data Format and Procedures Working Group*.

[Saastamoinen, 1973] Saastamoinen, J. (1973). Contributions to the theory of atmospheric refraction. *Bulletin Géodésique (1946-1975)*, 107(1):13–34.

[Seeber, 2003] Seeber, G. (2003). *Satellite geodesy*. Berlin [u.a]: De Gruyter, 2003.

[Sinclair, 1986] Sinclair, A. (1986). Satan-programs for the determination and analysis of satellite orbits for slr data. *SLR Technical Note*, 9:14.

[Svehla and Rothacher, 2003] Svehla, D. and Rothacher, M. (2003). Kinematic and reduced-dynamic precise orbit determination of low earth orbiters. *Advances in Geosciences*, 1:47–56.

[Tapley et al., 2004] Tapley, B. D., Bettadpur, S., Watkins, M., and Reigber, C. (2004). The gravity recovery and climate experiment: Mission overview and early results. *Geophysical Research Letters*, 31(9).

[Wahr, 1985] Wahr, J. M. (1985). Deformation induced by polar motion. *Journal of Geophysical Research: Solid Earth*, 90(B11):9363–9368.

[Wirnsberger et al., 2014] Wirnsberger, H., Krauss, S., and Baur, O. (2014). Contributions of satellite laser ranging to the precise orbit determination of low earth orbiters. In *Dragon 3Mid Term Results*, volume 724.

[Xu, 2010] Xu, G. (2010). *Sciences of geodesy*. Springer.

[Yan and Wang, 1999] Yan, H. and Wang, G. (1999). New consideration of atmospheric refraction in laser ranging data. *Monthly Notices of the Royal Astronomical Society*, 307(3):605–610.

[Yunck, 1992] Yunck, T. (1992). Chapter in precise orbit determination. *GPS WORLD*.

[Zehentner, 2017] Zehentner, N. (2017). *Kinematic orbit positioning applying the raw observation approach to observe time variable gravity*. PhD thesis, Institute of Geodesy (IfG), Graz University of Technology.